

Dissertation
submitted to the
Combined Faculties for the Natural Sciences and for Mathematics
of the Ruperto-Carola University of Heidelberg, Germany
for the degree of
Doctor of Natural Sciences

Put forward by

Ignacio Guillermo Espinoza Bornscheuer
Born in Osorno, Chile

Oral examination: 24th July 2013

Computer simulation of the radiation response of hypoxic tumours

Referees: Prof. Dr. Wolfgang Schlegel
Prof. Dr. Christian Karger

Zusammenfassung

In der Strahlentherapie ist es wichtig, die Strahlenreaktion von Tumoren vor der Behandlung vorhersagen zu können. Dies gilt insbesondere für hypoxische Tumoren, welche besonders strahlenresistent sind. Mathematische Modelle, die die Strahlenreaktion anhand von Dosisverteilung und biologischen Eingangsdaten für den Tumor simulieren, können helfen, diese Vorhersage zu verbessern und den Behandlungsplan zu optimieren. In dieser Arbeit wurde ein strahlenbiologisches Modell entwickelt, welches das Wachstum und die Strahlenreaktion von Tumoren unter Berücksichtigung von patientenspezifischen Informationen über den Tumor simuliert. Das Modell basiert auf Voxeln, die Tumor-, Kapillar-, Normal- und tote-Zellen beinhalten. Das strahleninduzierte Abtöten von Tumorzellen wird durch das linear-quadratische Modell berechnet (erweitert um Hypoxie zu berücksichtigen). Proliferation und Resorption von abgetöteten Zellen werden durch exponentielle Gesetze modelliert. Computertomographie, Positronen-Emissions-Tomographie und Kernspin-Tomographie können für die Charakterisierung des Tumors verwendet werden. Um hypoxische Tumoren zu simulieren, wurde besonderer Wert auf die Beschreibung der intratumoralen Sauerstoffversorgung gesetzt. Zu diesem Zweck wurde ein zweites komplementäres Modell entwickelt, das die mikroskopische Sauerstoffverteilung simuliert. Dieses Modell verwendet die vaskuläre Fraktion pro Voxel als Input Parameter, die im Prinzip nicht-invasiv in Patienten messbar ist, und macht Annahmen über die vaskuläre Architektur. Die Sauerstoff-Verteilung wird durch Lösen einer Reaktions-Diffusions-Gleichung unter Verwendung der *Particle Strength Exchange Methode* berechnet. Unter Berücksichtigung der Fraktionierung und der geplanten Dosisverteilung wird die raumzeitliche Entwicklung des Tumors simuliert. Das Modell beschreibt die Entwicklung von Hypoxie während des Tumorstwachstums sowie die Reoxygenierung während der Strahlentherapie. Neben anderen Parametern kann die Tumorkontrollwahrscheinlichkeit berechnet werden. Die Empfindlichkeit der Strahlenreaktion des Tumors auf die Werte der verschiedenen Parameter wird ebenfalls untersucht. Die Ergebnisse stimmen mit denen publizierter Studien überein. Vor einer klinischen Anwendung muss das Modell mit weiteren experimentellen und klinischen Daten validiert werden.

Abstract

In radiotherapy, it is important to predict the response of tumours to irradiation prior to the treatment. This is especially important for hypoxic tumours, which are known to be highly radio-resistant. Mathematical modelling based on the dose distribution and biological input parameters may help to improve this prediction and to optimize the treatment plan. In this work a radio-biological model was developed, which simulates the growth and the response to radiotherapy of tumours considering patient-specific information of the tumour. The model is based on voxels, containing tumour, capillary, normal and dead cells. Radiation-induced killing of tumour cells is calculated by the Linear-Quadratic Model (extended for considering hypoxia). Proliferation and resorption of cells are modelled by exponential laws. Computed tomography, positron emission tomography and magnetic resonance imaging may be used for the initial characterisation of the tumour. To simulate the response of hypoxic tumours properly, special emphasis was put on the description of the intratumoural oxygenation. For this, a second complementary model was developed to simulate the microscopic oxygen distribution, considering as input the vascular fraction per voxel, which is in principle measurable non-invasively in patients, and assuming certain vascular architectures. The oxygen distribution is obtained by solving a reaction-diffusion equation using the Particle Strength Exchange method. Including the fractionation regime and the planned dose distribution of the radiation treatment, the spatial-temporal behaviour of the tumour is simulated. The model describes the appearance of hypoxia during tumour growth and the reoxygenation processes during radiotherapy. Among other parameters, the tumour control probability can be calculated. The sensitivity of the tumour response on the values of different parameters is systematically studied. The results are in accordance with published results. Prior to clinical application, the model has to be further validated with experimental and clinical data.

Index

1	Introduction.....	1
2	Materials and Methods	5
2.1	Background	5
2.1.1	Interaction of radiation with matter	5
2.1.2	Radiobiology of tumours	8
2.1.2.1	Tumour growth	8
2.1.2.2	Tumour response to irradiation.....	9
2.1.2.3	Hypoxia in tumours	11
2.1.2.4	Fractionation and the 4 R's of radiotherapy	13
2.2	Tumour oxygenation model (TOM)	15
2.2.1	Oxygen reaction-diffusion equation.....	15
2.2.2	Numerical solution to the oxygen reaction-diffusion equation.....	16
2.2.3	Vascular architecture.....	18
2.2.3.1	Point-like vessels	19
2.2.3.2	Parallel linear vessels	19
2.2.3.3	Linear vessels in 3D	19
2.2.4	Simulations	20
2.2.4.1	Test of the implemented algorithm.....	20
2.2.4.2	Oxygen distribution for different vascular architectures and vascular fractions	21
2.2.4.3	Oxygen distributions for different vascular heterogeneities and vascular fractions	21
2.2.4.4	Acute hypoxia.....	21
2.2.4.5	Conditions of simulation	22
2.2.5	Comparison of intervessel distances (<i>IVD</i>) distributions with published experimental data	22
2.3	Tumour response model (TRM).....	22
2.3.1	Structure of the model	22
2.3.1.1	Input data to TRM	23
2.3.1.2	Tumour cell proliferation	26
2.3.1.3	Angiogenesis	26
2.3.1.4	Cell survival after irradiation.....	26
2.3.1.5	Resorption of dead cells.....	27
2.3.1.6	Exchange of cells between voxels.....	27

2.3.2	Generation and visualization of the results	29
2.3.3	Simulations	30
2.3.3.1	Tumour growth	30
2.3.3.2	Tumour shrinkage during radiotherapy.....	31
2.3.3.3	Tumour control probability.....	32
2.3.3.4	Restricted proliferation of very hypoxic tumour cells	33
2.3.3.5	Redistribution of dose.....	33
3	Results	35
3.1	Tumour oxygenation model (TOM).....	35
3.1.1	Test of the implemented algorithm	35
3.1.2	Oxygen distribution for different vascular architectures and vascular fractions.....	35
3.1.3	Oxygen distributions for different vascular heterogeneities and vascular fractions.....	37
3.1.4	Acute hypoxia	40
3.1.5	Comparison of <i>IVD</i> distributions with experimental data	40
3.2	Tumour response model (TRM).....	41
3.2.1	Tumour growth	41
3.2.2	Tumour shrinkage during radiotherapy	44
3.2.3	Tumour control probability	51
3.2.4	Restricted proliferation capacity of very hypoxic tumour cells	51
3.2.5	Redistribution of dose	53
4	Discussion	55
4.1	Tumour oxygenation model	55
4.1.1	Simulations	55
4.1.2	Model assumptions	57
4.2	Tumour response model	59
4.3	Methods for validation	61
4.4	Potential clinical application.....	63
5	Conclusions.....	65
6	Bibliography.....	67
7	Acknowledgements.....	73

1 Introduction

Cancer is already the leading cause of death in many developed countries and is set to become a major cause of morbidity and mortality in the coming decades in all regions of the world [7]. Radiotherapy and surgery have been the two most effective treatments for cancer, followed by chemotherapy. It is estimated that more than half of all cancer patients receive radiotherapy during their treatment [28]. For many tumour types, radiotherapy has shown to be effective for both achieving long-term control and for palliative care of patients.

Radiotherapy uses ionizing radiation to kill cancerous cells by damaging their deoxyribonucleic acid (DNA) molecules. Unfortunately, not only tumour cells are killed during radiotherapy; normal tissue may be affected as well. That is why a great effort has been made in the last century in developing techniques that attempt to conform the energy delivered by the radiation to the tumour while sparing surrounding normal tissue. The ideal case would be to give a therapeutically sufficient dose to the tumour and zero to the *surrounding* normal tissue, but this is technically impossible yet. Therefore the actual dose in the tumours is limited by the radiation tolerance of the normal tissues and the applied delivery techniques. The decision about the suitability of the dose distribution and delivery technique is currently based only on the experience of the radio oncologist and published clinical studies. The additional incorporation of knowledge on the biological state of the specific tumour (and its surrounding normal tissue) of the specific patient to be treated would be an important improvement in the radiation treatment planning.

Mathematical modelling of the effect of radiation on tumours and normal tissue may help to optimize radiation treatment planning. Several models for describing different relevant radiobiological phenomena have been developed during the last decades, using parameters values that are obtained typically by fitting data from experimental and clinical studies. Some of the issues approached by these models are the influence of tumour growth, cell radiosensitivity and oxygen effect on tumour control probability (TCP) as well as the modelling of normal tissue complication probability (NTCP). These existing models, together with tumour- and patient-specific information, can be used in a combined form to assess the effect of the radiation treatment in the individual patient.

Additionally to the sophisticated dose delivery techniques existing nowadays and the mathematical models previously mentioned, cancer imaging is an essential tool for radiotherapy. It not only allows visualizing tumour anatomy, but also characterizes the biological status of the tumour. Several imaging techniques that give morphological

and/or functional information about tumours have been developed during the last century and are currently available in the majority of the hospitals. Radiography, computed tomography (CT), ultrasonography, magnetic resonance imaging (MRI), positron emission tomography (PET) and single-photon emission computed tomography (SPECT) are the most common medical imaging techniques used in relation to radiotherapy. These, together with the use of mathematical models, may help to improve the prediction and the assessment of the effects of radiotherapy and therefore to optimize the treatment.

The objective of this work was to develop a computational model for simulating tumour growth and tumour response to radiotherapy, under consideration of relevant tumour- and patient-specific biological information. The developed model is termed Tumour Response Model (TRM) and considers clinical tumours, i.e. of any shape and size, by separating the virtual tumour in voxels that contain 4 different types of cells: tumour, normal, dead and capillary cells. During the initialization of the virtual tumour, patient-specific information, obtained from medical imaging (CT, PET and/or MRI), as well as tumour-specific radiobiological parameters can be taken into consideration. After the initialization, the temporal development of the tumour is simulated, considering the most important radiobiological mechanisms, like tumour cell proliferation, hypoxia induced capillary cell proliferation (angiogenesis), radiation-induced tumour cell killing and resorption of dead cells. The TRM considers typical dose distributions and fractionation schemes, as well as three different types of material surrounding the tumours: soft tissue, bone and air.

Because hypoxia plays a key role in the assessment of the tumour response to radiotherapy, especially due to the dependence of radiosensitivity of tumour cells on the oxygenation level, a second model was developed for simulating the 3D microscopic distribution of oxygen in tumour voxels. This model is termed Tumour Oxygenation Model (TOM) and is able to calculate oxygenation histograms for each tumour voxel, using as input the vascular fraction and making reasonable assumptions about vascular architecture and oxygen blood content. Using the results of the TOM, the TRM is able to simulate the influence of oxygen on the tumour radiation response.

This further develops the model by Harting *et al.*[26], which simulates the tumour response on the basis of the response of individual tumour cells by Monte-Carlo methods. This model was restricted to small spherical tumours and made several simplifications about the distribution of oxygen. Works published later motivated the separation of the tumour into subvolumes (voxels) containing a large number of cells [19] and the use of medical imaging techniques, like PET, to incorporate patient-specific information about oxygenation and proliferation [70]. The development of TOM was mainly motivated by the model published by Dasu *et al.*[14], who simulated oxygen distribution in tumours by

solving a reaction-diffusion equation, considering a simplified heterogeneous 2D vascular architecture. In contrast to Dasu's model, some features unique to TOM include the use of a new numerical calculation method, the ability of simulating in three dimensions, the incorporation of the vascular fraction as an input parameter, the use of very heterogeneous vessels distributions (according to experiments), and the possibility of simulating hypoxemic acute hypoxia.

Following this introduction, chapter 2 starts with a brief background section, in which relevant aspects about the interaction of radiation with matter and the radiobiology of tumours are presented. Then, the details about the implementation of both TOM and TRM are explained. The different simulations that were done are described as well. Chapter 3 presents the results obtained using TOM and TRM and chapter 4 contains a discussion on the obtained results. Finally, chapter 5 presents the conclusions of this work.

2 Materials and Methods

2.1 Background

2.1.1 Interaction of radiation with matter

Radiation is classified into two main categories: non-ionizing and ionizing [53]. Only the later is relevant for radiotherapy, because the biological effect of radiation is caused by ionization of bio-molecules in the cells. Ionizing radiation can be classified into two categories as well: directly and indirectly ionizing radiation. Charged particles, like electrons, protons, α particles and heavy ions belong to the first category. Neutral particles, like photons and neutrons, belong to the second one. This work considers radiotherapy with X-rays (photons), because this is the most frequently used radiation modality in the world. Therefore, emphasis is put on the description of this type of interaction. Nevertheless, even if the primary radiation is a photon beam, it is the charged particles (mainly electrons), known as secondary radiation, which finally transfer the energy to the cells and cause the biological effect [39].

Charged particles deposit their energy quasi-continuously in the tissue by means of direct Coulomb interactions with atomic orbital electrons and atomic nuclei. By interacting with orbital electrons, they create a track of ionizations and excitations along their paths, and interactions with nuclei result in the production of either bremsstrahlung or elastic nuclear scattering. During these processes, charged particles may lose energy and/or change their travel direction [39, 53].

Photon interactions with matter are of stochastic nature, i.e. photons may undergo few, one, or no interaction as they pass through matter [39]. Depending on the photon energy and the atomic number of the medium, photons have different probabilities (given by the cross-sections) of undergoing the following interactions [39, 53]:

- **Photoelectric absorption.** The photon interacts with a bound electron of the medium and is absorbed. The electron receives all its energy ($h\nu$) and leaves the atom, as a photo-electron, with a kinetic energy given by $T = h\nu - E_B$, where E_B is its binding energy. In general, despite some discontinuities (absorption edges) corresponding to the binding energies of the K, L, etc. atomic shells, the cross-section per atom σ_{ph} decreases strongly with the increasing photon energy. It also increases strongly with increasing atomic number of the medium ($\sigma_{ph} \propto Z^4/(h\nu)^3$). In case of low energetic photons, photoelectrons are more likely ejected at directions perpendicular to the direction of the photon. For larger

energies, this angular distribution becomes forward directed. The vacancy left in the atomic shell is filled by another electron coming from outer shells and the energy difference is emitted in form of a photon (characteristic x-rays) or an Auger electron.

- **Coherent (Rayleigh) scattering.** This is the name of the process in which the photon is collectively scattered by the electrons of the atom through small angles losing essentially no energy. Therefore, it contributes only to the photon attenuation but not to the energy transfer. For the energies used in radiotherapy, Rayleigh scattering is of minor importance, relative to other photon interactions. The corresponding cross-section per atom is proportional to $(Z/h\nu)^2$.
- **Compton interaction (incoherent scattering).** The Compton is the most important interaction process in radiotherapy and occurs when the energy of the incident photon, $h\nu$, is much larger than the binding energy of the electrons in an atom. In this case, the electron is assumed to be free and at rest. The incident photon is scattered through an angle θ and the energy of the scattered photon is given by:

$$h\nu' = \frac{h\nu}{1 + \alpha(1 - \cos \theta)} \quad (2.1)$$

where $\alpha = h\nu/(m_e c^2)$ and m_e is the rest mass of the electron. For $\theta = 0$ there is no energy transfer to the electron and the energy transfer is maximal in case of backscattering ($\theta = 180^\circ$). The fraction of energy transfer increases with increasing photon energy. The angle between the incoming photon and the outgoing electron (ϕ) is given by $\cot \phi = (1 + \alpha) \tan(\theta/2)$. The possible range for ϕ is from 0 (for $\theta = 180$) to 90° (for $\theta = 0$) and the angle ϕ decreases by increasing incident photon energy, for fixed θ . The atomic cross-section is proportional to Z and decreases steadily with $h\nu$. The relativistic cross-section is named after Klein and Nishina, who first derived it.

- **Pair and triplet production.** If a photon has energy $h\nu$ larger than $2m_e c^2 = 1.02$ MeV, it can be absorbed by the electric field of the nucleus and an electron-positron pair is created. The sum of the kinetic energies of these two particles is $h\nu - 2m_e c^2$ and they tend to travel in the forward direction. The positron annihilates then with an electron and two photons of energy 511 keV are emitted in opposite directions. The atomic cross-section is zero for energies below the threshold and increases rapidly with $h\nu$ above the threshold. For large energies, it is approximately proportional to Z^2 . If the pair production occurs in the field of an orbital electron instead of the nucleus, the effect is called triplet production. In this case, the bound electron recoils with enough energy to leave the atom and therefore the energy of the incident photon is shared by three particles. The cross-

section is proportional to Z . Therefore, it has comparable importance as pair production for hydrogen, but it becomes less important for larger atomic numbers [39].

- **Nuclear photoeffect.** Also called photonuclear or photodisintegration reaction, it occurs when an incident photon has more energy than the binding energy of a nucleon. The nucleus can then absorb the photon, emit one or more protons or neutrons, and become radioactive. Nuclear photoeffect usually occurs for energies larger than 10 MeV. Nevertheless, its probability of occurrence is small compared with other photon interactions.

In radiotherapy, only photoelectric absorption, Compton interaction and pair production play a significant role. Figure 2.1 shows the relative predominance of these three interactions as a function of the atomic number and the photon energy.

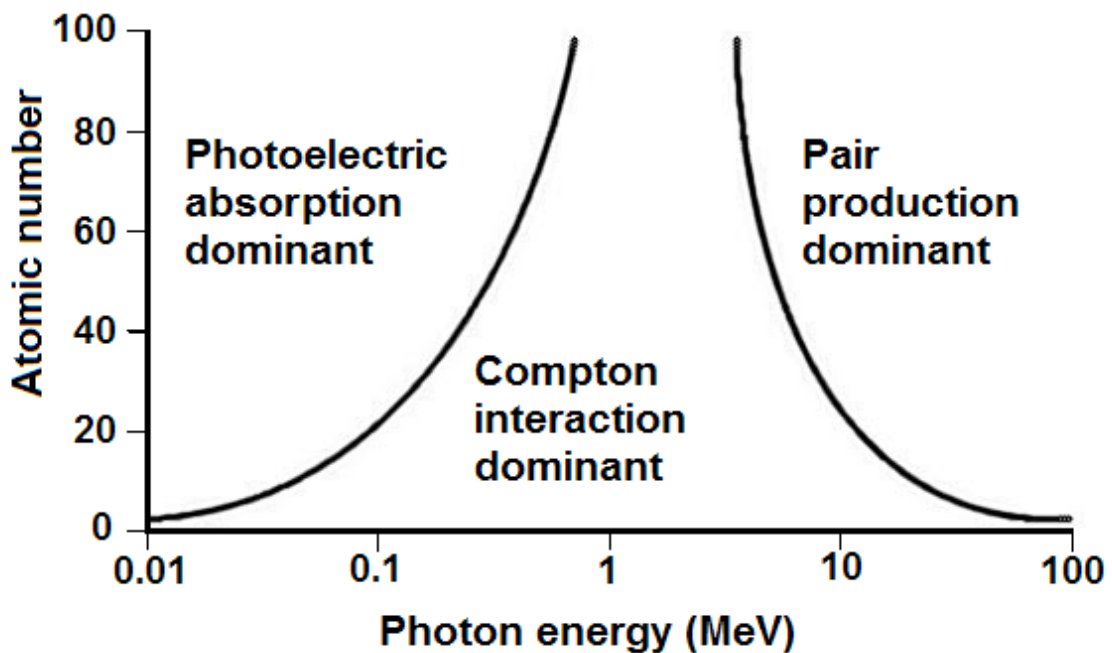


Figure 2.1: Relative predominance of the three most important photon interactions with matter. The left (right) line indicates the border at which the cross sections of photoelectric absorption and Compton interaction (Compton interaction and Pair production) take the same value [53].

In radiotherapy, the Compton interaction is dominant, because the photon energies normally used are in the range of a few MeV to about 20 MeV, and because the human body is composed to a great extent of water, which has low atomic numbers.

It is common to describe the photon interactions with matter macroscopically by beam attenuation. Beam attenuation can be theoretically described as follows. For a given mono-energetic beam crossing a thin layer, dx , of attenuating material, the number of

primary photons, $d\Phi$, that interact with the layer is proportional to dx and to the number of incident photons. This can be written in the following form:

$$d\Phi = -\mu dx\Phi(x) \quad (2.2)$$

where μ , the so-called linear attenuation coefficient, depends on the material and the beam energy. The minus sign indicates that the photons that interact with the material leave the incident beam. Assuming a monoenergetic beam, expression (2.2) can be integrated to consider an arbitrarily thick layer of thickness d :

$$\Phi(d) = \Phi(0)e^{-\mu d} \quad (2.3)$$

where $\Phi(0)$ is the number of incident photons. μ is the interacting probability of the photon per length unit, and corresponds therefore to the product of the total atomic cross-section with the number of targets (atoms) per volume [39].

A very important quantity in radiotherapy is the absorbed dose, D . It is defined as the mean energy $\bar{\epsilon}$ imparted by ionizing radiation to matter of mass m in a finite volume V by:

$$D = \frac{d\bar{\epsilon}}{dm} \quad (2.4)$$

$\bar{\epsilon}$ is the sum of the energy entering the volume, minus the energy leaving it, taking into account any mass-energy conversions [53]. The unit of the absorbed dose is the Gray (Gy), where $1 \text{ Gy} = 1 \text{ J/kg}$.

2.1.2 Radiobiology of tumours

2.1.2.1 Tumour growth

A tumour is defined as an abnormal new growth of tissue that possesses no physiological function and arises from uncontrolled, usually rapid, cellular proliferation [41]. This growth is the result of a disturbed tissue homeostasis, driven by capabilities acquired during tumourigenesis, like self-sufficiency in growth signals, insensitivity to anti-growth signals, limitless proliferative potential, evading apoptosis (programmed cell death) and sustained angiogenesis (formation of new blood vessels) [28]. The cellular proliferation is determined by the cell proliferation cycle, which describes the changes that the cells undergo between two divisions. The cell cycle has four well-defined phases: G1, S, G2 and M. After a cell division, the first phase is the G1-phase, in which the cell grows. In the S-phase, the DNA is synthesised. The G2-phase is similar to G1. Here the cell continues growing and preparing DNA for the mitosis (M-phase), where division takes place. This

cycle is repeated continuously with a period of several hours to a few days, depending on the type of cell, leading to an exponential growth. In macroscopic tumours, however, this exponential growth is limited because of a lower proportion of cycling cells, a prolongation of cell cycle and/or a higher cell death rate [28].

Angiogenesis is a crucial process that allows large (clinical) tumours to grow. Cells need nutrients and oxygen to proliferate, and these are received from nearby vasculature through diffusion when the tumours are sufficiently small. When the tumour radius becomes larger than the diffusion distances of nutrients and oxygen, some cells become insufficiently supplied and produce VEGF (vascular endothelial growth factor), a signal protein that travels to nearby vessels and induces vascular growth. The new vessels grow into the tumour, bringing oxygen and nutrients, and therefore allowing the proliferation of cells located far from the tumour surface. Nevertheless, this process is not fast and effective enough to counteract the faster tumour growth, and therefore hypoxic regions appear (see section 2.1.2.3).

2.1.2.2 Tumour response to irradiation

Radiation damage and repair

Radiation damage can be classified into two categories: direct and indirect. Direct damage is caused when atoms of the target itself (DNA) are ionized or excited through Coulomb interactions [53]. Indirect damage is caused by free radicals that are produced by ionization and excitation of other molecules in the cell. Because water is the most prevalent molecule within the cell, most of the free radicals are produced by radiolysis of water [39]. Free radicals react easily with nearby molecules, producing chemical damage. All components of the cell may be damaged, but all molecules, apart from DNA, are available in great number within the cell and therefore damage to a few of them does not compromise the cell's viability. However, the DNA molecules are unique and when they are damaged, the vital cell's functions are endangered. This is why DNA is the most vulnerable part of the cell. The three most relevant types of DNA damage are:

- **Base damage:** one or several bases of the DNA are lost or modified, but the complementary bases remain intact.
- **Single strand break (SSB):** only one of the two strands of the double helix has a defect.
- **Double strand break (DSB):** both strands of the double helix have a defect.

There are very efficient DNA repair processes. As an example, a dose of 1 Gy causes in each cell approximately 10^5 ionizations, more than 1000 base damages, around 1000 SSBs and around 20-40 DSBs, however only about 30% of the cells are killed at this dose [28].

Cells that cannot be properly repaired may die before mitosis or after several cell cycles, or survive with mutations, which may lead to transformed phenotypes and possible carcinogenesis [53]. Dead cells are resorbed through phagocytosis by adjacent cells or macrophages.

The Linear-Quadratic (LQ-) model

The survival fraction (SF) of cells irradiated with a single dose d is usually described by the Linear-Quadratic model [53]:

$$SF = e^{-(\alpha d + \beta d^2)} \quad (2.5)$$

α and β are parameters fitted from experimental data and represent the amount of lethal and sub-lethal cell damage, respectively [58, 39]. In a logarithmic representation, SF is described by a linear-quadratic curve, the so-called cell survival curve. Lethal damage cannot be repaired; sub-lethal damage is repaired, normally within less than 6 hours. This repair ability motivates the use of a fractionated dose delivery (see section 2.1.2.4).

Tumour control probability (TCP)

A tumour is assumed to be controlled if none of the clonogenic tumour cells (cells that are able to proliferate and form new tumours) survive [46]. TCP has been mathematically modelled assuming that tumours consist of a number of non-interacting clonogenic cells, which respond independently to irradiation. The probability that k out of N clonogenic cells survive after the irradiation is given by binomial statistics, and may be approximated for large N and constant $N \cdot SF$ by Poisson statistics [58]:

$$P(k) = \binom{N}{k} SF^k (1 - SF)^{N-k} \approx \frac{(N \cdot SF)^k}{k!} e^{-N \cdot SF} \quad (2.6)$$

TCP corresponds to $P(0)$, so:

$$TCP \approx e^{-N \cdot SF} \quad (2.7)$$

where SF is usually given by the LQ-model (equation (2.5)). This model can be extended to consider heterogeneities in radiosensitivity and dose distributions by dividing the tumour into sub-regions. Some temporal phenomena, like repopulation, can be additionally considered by extending the LQ-model. However, more complex phenomena, like angiogenesis and hypoxia, are impossible to describe properly using this statistical model. An alternative approach to assess TCP considering these complexities is the model presented in this work.

2.1.2.3 Hypoxia in tumours

Due to the fact that angiogenesis is not able to counteract the rapid growth of tumours (see section 2.1.2.1), the new vasculature (normally morphologically and functionally abnormal) is unable to supply the oxygen demand properly, leading to the appearance of hypoxic regions [28]. Hypoxia in tumours can be classified into two categories:

- **Chronic (diffusion-limited) hypoxia**, which happens when the distance of oxygen-consuming cells from the vessels is larger than the maximum diffusion distance of oxygen.
- **Acute (perfusion limited) hypoxia**, which refers to the transient hypoxia of cells due to intermittent changes in blood flow or oxygen content in tumour vessels. The mechanisms responsible for this kind of hypoxia are currently not fully clear.

There are four types of heterogeneity associated with hypoxia [28]:

- **Heterogeneity in severity.** Cells exist in all possible oxygen concentrations, from normoxic to anoxic.
- **Heterogeneity in space.** Steep gradients of oxygen concentration can exist over distances of only a few cell diameters.
- **Heterogeneity in time.** Cells can experience both slow and fast changes in oxygenation levels. Slow changes occur when cells move through an oxygenation gradient given by chronic hypoxia. Fast changes occur due to acute hypoxia.
- **Heterogeneity amongst patients.** Oxygenation differs markedly among patients.

Hypoxia is important for radiotherapy because hypoxic cells are more resistant to radiation [24]. The oxygen fixation hypothesis explains the mechanism that causes this effect: in the presence of oxygen, the radiation-induced free radicals created in DNA, R' (see section 2.1.2.2), react easily with oxygen, forming organic peroxide RO_2 , which ultimately yields the organic hydroperoxide $ROOH$. This corresponds to a stable chemical change in the DNA molecule and therefore the damage is said to be 'fixed'. If no oxygen or little is present, R' molecules have a longer half-life and can react with H^+ , thus chemically restoring their original form [28]. Figure 2.2 shows the difference between survival curves of hypoxic and oxic irradiated cells.

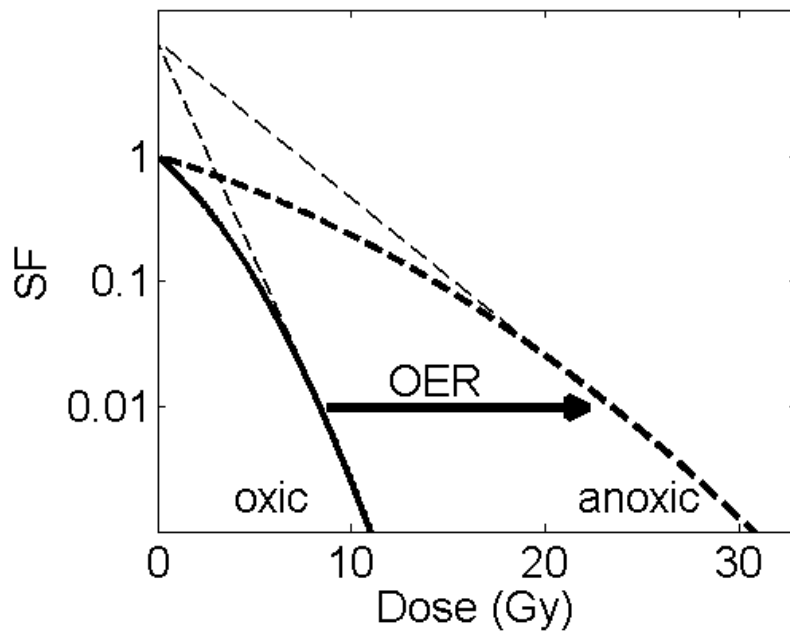


Figure 2.2: Example of survival curves under oxic and anoxic conditions. The broken lines extrapolate back to the same point on the vertical axis.

The oxygen enhancement ratio (OER) is defined as the ratio of doses with and without oxygen that produce the same biological effect [53]:

$$OER = \frac{\text{Dose to produce a given effect without oxygen}}{\text{Dose to produce the same effect with oxygen}} \quad (2.8)$$

Most cell types have an *OER* value of around 3 for x-ray irradiation under oxic conditions (some studies have suggested smaller values in case of doses smaller than 3 Gy [50, 10, 45], but this is currently not fully understood). This means that one needs approximately a 3 times higher dose to achieve the same effect in hypoxic as compared to oxic cells. For intermediate levels of oxygenation, the *OER* may be parameterized as a function of the oxygen partial pressure [1]:

$$OER(P_{O_2}) = \frac{mP_{O_2} + k}{P_{O_2} + k} \quad (2.9)$$

where *m* and *k* are constants. Figure 2.3 shows this dependency graphically. For hypoxic conditions the *OER* is close to 1 and it approaches the maximum value for oxygen partial tensions larger than 10-20 mmHg. The oxygen effect is thus relevant for oxygenation levels below this threshold.

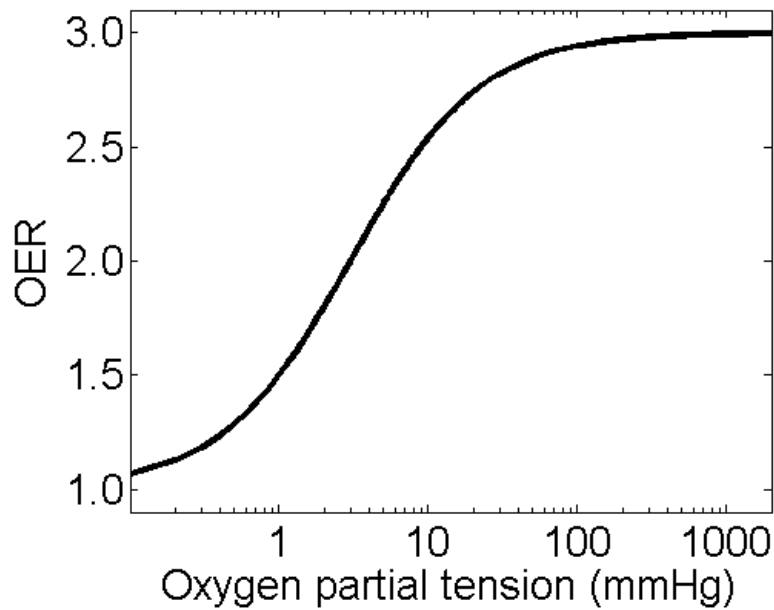


Figure 2.3: OER dependence on oxygen partial tension [75].

Equation (2.8) can be integrated in equation (2.5) to obtain a P_{O_2} -dependent survival fraction:

$$SF = e^{-\left(\frac{\alpha}{m}d \cdot OER(P_{O_2}) + \frac{\beta}{m^2}d^2 OER(P_{O_2})^2\right)} \quad (2.10)$$

where α and β now refer to oxic conditions [26].

2.1.2.4 Fractionation and the 4 R's of radiotherapy

As mentioned in section 2.1.2.2, sub-lethal damage can be repaired within a few hours after irradiation. This repair capacity is normally better for normal tissue (especially for late-responding normal tissue) than for tumours, motivating thus a fractionated delivery of the dose, with pauses sufficiently large to allow this repair. To achieve a certain level of biological effect, however, the total dose must be larger in a fractionated treatment than in a single-dose treatment. But the repair capacity of normal and tumour cells is not the only factor determining the radiation response in fractionated radiotherapy. Four main biological factors must be considered. These are the so-called “4 R's of radiotherapy”:

- **Repair.** Enzymes can repair radiation damage within a few hours after radiation exposure.
- **Redistribution (or reassortment).** Cells in different cell cycle phases show different radiosensitivities (in increasing order of sensitivity: S, G1, G2 and M), leading to a certain synchronization in the cells right after irradiation (the majority of the cells that survive are in the more resistant phases). Through the redistribution process,

surviving cells leave this hyperresistant state at different times and with increasing time recover the distribution over the cell cycle, which was present before irradiation [28].

- **Repopulation.** Surviving tumour cells proliferate during the course of radiotherapy, leading to an increased number of cells to be killed.
- **Reoxygenation.** Surviving radioresistant hypoxic cells become less resistant due to an improvement of their oxygen supply after the irradiations.

While repair and repopulation make tissues more resistant, redistribution and reoxygenation make them more sensitive. These factors have to be considered in the design of fractionation regimes. Currently, five fractions of 2 Gy per week over 6-7 weeks is the standard fractionation schedule. However, other fractionation regimes are being studied and could be used for achieving certain purposes. Some relevant examples are:

- **Hypofractionated treatment** is the use of fewer fractions with a higher dose per fraction. This approach has been used traditionally in palliative radiotherapy; however its use in curative radiotherapy has increased due to the development of techniques that precisely target the tumours by sparing normal tissue, like stereotactic body radiation therapy (SBRT). Hypofractionated treatments are often associated with a shortening of the overall treatment time (accelerated treatments, see below).
- **Hyperfractionated treatment** means more fractions per day with reduced dose per fraction. This approach may be used to reduce late normal tissue effects when applying an increased total dose.
- **Accelerated treatment** consists of a reduced overall treatment time that minimizes repopulation of tumour cells. This can be achieved by hypofractionated or by hyperfractionated treatments.

2.2 Tumour oxygenation model (TOM)

2.2.1 Oxygen reaction-diffusion equation

As in several previous studies [14, 32, 3, 42], the distribution of oxygen within the tumour in case of diffusion-limited hypoxia is modelled using a reaction-diffusion equation:

$$\frac{\partial u(\mathbf{x}, t)}{\partial t} = D\Delta u(\mathbf{x}, t) - g(u(\mathbf{x}, t)), \quad (2.11)$$

where $u(\mathbf{x}, t)$ is the spatio-temporal distribution of the oxygen concentration and g describes the oxygen consumption rate of the tissue, which in general may depend on the available oxygen concentration $u(\mathbf{x}, t)$. D is the diffusion coefficient. The temporal variation of u in every point is determined by the flux of oxygen molecules due to the concentration gradient and by the oxygen consumption of the cells in the tissue, given by the first and the second term of the right side of Equation (2.11), respectively.

In Equation (2.11), the tumour is treated as a continuum. For modelling the oxygen distribution in tumours, it has been shown to be a reasonable approximation to treat D as a scalar with a fixed average value [54, 14]. This means that the diffusion is considered to be isotropic and homogeneous. Furthermore, using the proportionality between the concentration and the partial pressure given by Henry's law ($P = k_H u$) and assuming a constant temperature, k_H can be considered to be constant and Equation (2.11) can then be rewritten by replacing the concentration u by the oxygen partial pressure P . The oxygen consumption rate is modelled by the Michaelis-Menten kinetics [59, 21, 14], which can be expressed as:

$$g(P_{O_2}(\mathbf{x}, t)) = g_{\max} \frac{P_{O_2}(\mathbf{x}, t)}{P_{O_2}(\mathbf{x}, t) + k}. \quad (2.12)$$

For high oxygen levels the consumption rate is practically constant while it decreases for lower oxygen concentrations, consistent with the findings of Tang [66]. Here, g_{\max} is the maximum oxygen consumption rate and k the oxygen pressure at which the consumption rate is half of g_{\max} . In this study, the following parameter values were used: $D = 2 \cdot 10^{-9} \text{m}^2 \text{s}^{-1}$, $g_{\max} = 15 \text{mmHg s}^{-1}$ and $k = 2.5 \text{mmHg}$ [67, 11, 14].

For the simulation of the oxygen distribution, the tumour was assumed to consist of vessels being the sources of oxygen supply and tumour cells outside the vessels consuming the oxygen. Within the vessels, the oxygen partial pressure is assumed to be constant in time, which leads to stationary conditions after a certain time period. As the oxygen supply in tumours usually originates from venules [72], a fixed value of 40 mmHg is used for the oxygen concentration within the vessels [61], if not otherwise specified.

Similarly to other published studies [14, 30, 42], variations of oxygen partial pressure along the vessels were neglected.

For a given vascular fraction, vessel diameter, vessel architecture, and heterogeneity, the steady state solution of Equation (2.11) was obtained numerically using the Particle Strength Exchange (PSE) method (see section 2.2.2). As a result, a map of the oxygen distribution and PO2 histograms were obtained.

2.2.2 Numerical solution to the oxygen reaction-diffusion equation

Equation (2.11) is solved in Matlab (The Mathworks Inc., MA, USA) by the implementation of the Particle Strength Exchange (PSE) method. The PSE method is a deterministic particle method to simulate diffusion in space. It is based on the approximation of the Laplacian operator by an integral operator and was described and studied by Degond and Mas-Gallic [15] and Cottet and Koumoutsakos [12].

It can be shown that a mass-conserving integral approximation of the Laplace-operator over an intensive quantity (i.e. the concentration) u is given by [15]:

$$\Delta_\varepsilon u(\mathbf{x}) = \frac{1}{\varepsilon^2} \int_{\mathbb{R}^{\bar{D}}} (u(\mathbf{y}) - u(\mathbf{x})) \eta_\varepsilon(\mathbf{y} - \mathbf{x}) d^{\bar{D}}\mathbf{y} , \quad (2.13)$$

where η_ε is a kernel function $\eta_\varepsilon(\mathbf{x}) = \varepsilon^{-\bar{D}} \eta(\mathbf{x}/\varepsilon)$ of width $\varepsilon > 0$ in \bar{D} spatial dimensions that satisfies certain moment properties [12]. ε is a measure of the range of interactions of every voxel with its neighbourhood; the larger ε is, the more neighbouring voxels are interchanging oxygen molecules. For our purposes \bar{D} can be 2 or 3 for simulations in a plane or in a volume, respectively. Equation (2.13) can be discretized as follows:

$$\Delta_\varepsilon u(\mathbf{x}_p) = \frac{1}{\varepsilon^2} \sum_{q=1}^N (V_q u(\mathbf{x}_q) - V_q u(\mathbf{x}_p)) \eta_\varepsilon(\mathbf{x}_q - \mathbf{x}_p), \quad (2.14)$$

where V_q stands for the volume of the q -th particle. In the context of the PSE-method, a particle is considered as a volume containing a certain number of oxygen molecules (its strength) and may be either static or moving in space. Here, all particle volumes are considered to be equal ($V_q = V$), so equation (2.14) can be expressed in terms of the extensive quantity $\omega(\mathbf{x}_p) = V u(\mathbf{x}_p)$:

$$\Delta_\varepsilon \omega(\mathbf{x}_p) = \frac{V}{\varepsilon^2} \sum_{q=1}^N (\omega(\mathbf{x}_q) - \omega(\mathbf{x}_p)) \eta_\varepsilon(\mathbf{x}_q - \mathbf{x}_p), \quad (2.15)$$

where $\omega(\mathbf{x}_p)$ is the number of oxygen molecules in particle p . The kernels in \mathbb{R}^2 and \mathbb{R}^3 are given by [57]:

$$\eta_\varepsilon(\mathbf{x}_p - \mathbf{x}_q) = \frac{4}{\varepsilon^2 \pi} e^{-\frac{\|\mathbf{x}_p - \mathbf{x}_q\|^2}{\varepsilon^2}} \quad (2.16a)$$

and

$$\eta_\varepsilon(\mathbf{x}_p - \mathbf{x}_q) = \frac{4}{\varepsilon^3 \pi^{3/2}} e^{-\frac{\|\mathbf{x}_p - \mathbf{x}_q\|^2}{\varepsilon^2}} \quad (2.16b)$$

respectively, where $\|\mathbf{x}_p - \mathbf{x}_q\|$ is the Euclidian distance between \mathbf{x}_p and \mathbf{x}_q . For the problem considered here, the positions of the particles do not change with time (i. e. $\frac{\partial \mathbf{x}_p}{\partial t} = 0, \forall p$) and the particles are therefore static in space. In this case, the dynamics of the particle strength considering only diffusion (without influence of sources and consumption of oxygen) is then given by:

$$\left. \frac{\partial \omega(\mathbf{x}_p, t)}{\partial t} \right|_{\text{diffusion}} = \frac{VD}{\varepsilon^2} \sum_{q=1}^N (\omega(\mathbf{x}_q, t) - \omega(\mathbf{x}_p, t)) \eta_\varepsilon(\mathbf{x}_q - \mathbf{x}_p). \quad (2.17a)$$

As the oxygen consumption term of Equation (2.11) depends only on the local oxygen partial pressure, the dynamics of the particle strength due to the oxygen consumption can be directly calculated from Equation (2.12):

$$\left. \frac{\partial \omega(\mathbf{x}_p, t)}{\partial t} \right|_{\text{consumption}} = g_{\max} \frac{\omega(\mathbf{x}_p, t)}{\omega(\mathbf{x}_p, t) + k}. \quad (2.17b)$$

Since the oxygen partial pressure in capillaries is considered constant, the dynamics of the particle strength corresponding to particles located in capillaries is simply:

$$\left. \frac{\partial \omega(\mathbf{x}_p, t)}{\partial t} \right|_{\text{capillaries}} = 0 \text{ or } \omega(\mathbf{x}_p, t) = \omega_{\text{cap}}, \forall t. \quad (2.17c)$$

After generating a certain capillary architecture in a reference volume (see section 2.2.3 for details), the oxygen distribution is calculated using particle strength dynamics of Equations (2.17a)-(2.17c). For time step n and for every particle p , the contribution $\partial \omega$ of the different processes is calculated iteratively as follows:

$$\delta\omega_{p,\text{diffusion}}^n = \frac{VD\delta t}{\varepsilon^2} \sum_{q=1}^N (\omega_q^n - \omega_p^n) \eta_\varepsilon(\mathbf{x}_q - \mathbf{x}_p) \quad (2.18a)$$

$$\delta\omega_{p,\text{consumption}}^n = \delta t g_{\max} \frac{\omega_p^n}{\omega_p^n + k} \quad (2.18b)$$

As a result the strength of particle p at time step $n+1$ is calculated according to:

$$\omega_p^{n+1} = \omega_p^n + \delta\omega_{p,\text{diffusion}}^n + \delta\omega_{p,\text{consumption}}^n \quad (2.19a)$$

According to the prerequisite that the oxygen concentration within the capillaries is fixed, the particle strength within the capillaries is set back to its initial value after each iteration:

$$\omega_p^{n+1} = \omega_p^n = \omega_{\text{cap}}, \quad \forall p \text{ in capillaries} \quad (2.19b)$$

To handle missing contributions from particles outside the reference volume, periodic boundary conditions were used. In addition, Verlet lists were used to accelerate the computation [73]. The iterations were stopped when a steady state was approximately achieved.

2.2.3 Vascular architecture

Vessels were placed on a cubic grid in a reference volume, V_{ref} (usually corresponding to a tumour voxel), by defining certain volume elements as vessel elements. While vessel elements are considered as small sources of oxygen located on a grid position, several of the vessel elements may be connected to form linear structures, which are termed vessels in the framework of this model. The number of vessel elements N to be distributed within the reference volume is specified by the vascular fraction vf :

$$N = vf \cdot \frac{V_{ref}}{V} \quad (2.20)$$

where V is the volume of the volume element. To study the relation between the distribution of vessel elements and the corresponding oxygen distribution, three different vascular architectures were considered (Figure 2.4).

2.2.3.1 Point-like vessels

In the simplest case, N vessel elements are distributed randomly over the reference volume (Figure 2.4a). A uniform probability distribution was used to choose the coordinates of the position of each of these single vessel elements. Similar approaches of point-like vessel elements have been used previously by other authors [5, 26].

2.2.3.2 Parallel linear vessels

A more realistic approach to model the vessel architecture is when the vessel elements form elongated structures. Considering linear vessels, parallel to each other, the 3D problem is reduced to a 2D problem (Figure 2.4b), which is of advantage with respect to the calculation time. This type of vessel architecture was used previously by Daşu *et al.* [14] to simulate the oxygen distribution in two dimensions.

Construction of the parallel linear vessel architecture was performed as follows: First, the number of vessel elements, N , was rounded to form an integer number of linear vessels crossing the complete reference volume. Secondly, the vessels were distributed within the reference volume using two alternative methods: (i) completely randomly distributed following a uniform probability distribution (Figure 2.5a), or (ii) partially randomly distributed. In the second case, vessels are first placed on a regular grid (Figure 2.5b) with constant intervessel distances (IVD_0). Then, the position of each vessel is varied according to a normal distribution $N(x, \sigma)$, centred on the initial vessel position x and having the standard deviation σ . For small values of σ , the distribution of vessels is fairly regular (Figure 2.5c) and becomes increasingly similar to the completely randomly distributed pattern of Figure 2.5a as σ becomes larger (Figure 2.5d). The parameter σ may be used to specify the heterogeneity of the vessel architecture for a given number of vessels (i.e. vascular fraction). In this work, the vessels were distributed according to method (i) unless otherwise specified.

2.2.3.3 Linear vessels in 3D

As a further step towards the complexity of real tumours, the linear vessels were oriented in the three directions of space (Figure 2.4c). The orientation of each vessel is selected randomly. Otherwise, the distribution of the vessels within each of the three perpendicular planes is performed in the same way as in the case of parallel-linear vessels in 2D.

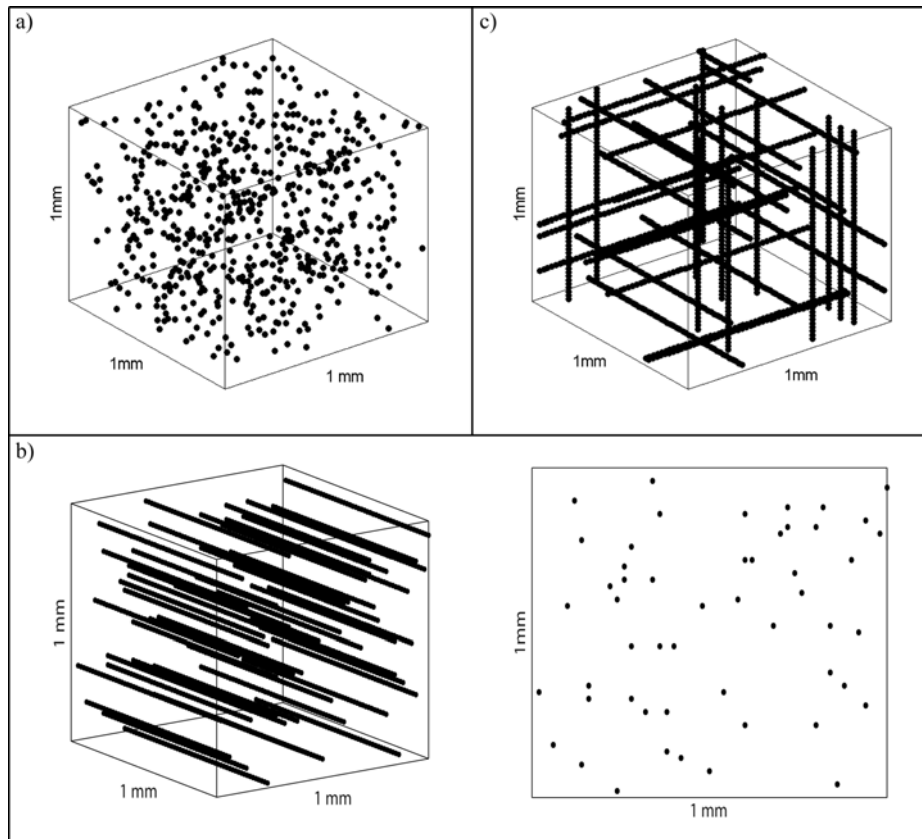


Figure 2.4: Three types of vascular architecture: a) point-like vessels, b) parallel linear vessels (in a 3D view and a 2D-projection) and c) linear vessels in 3D.

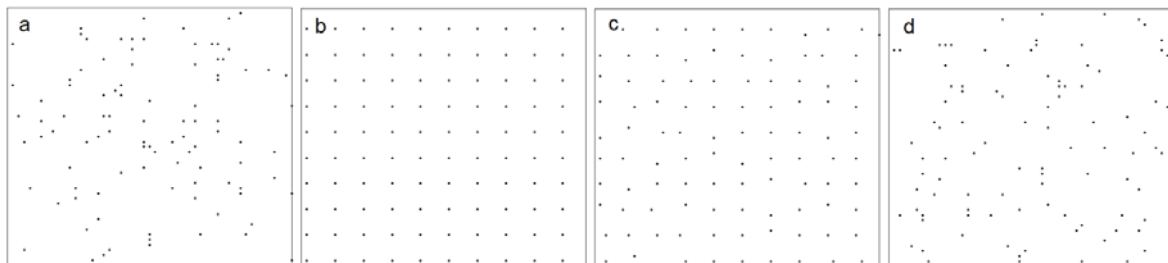


Figure 2.5: Distributions of parallel linear vessels: completely randomly distributed pattern (a) and partially randomly distributed pattern with $\sigma = 0$ (b), $\sigma = IVD_0/10$ (c) and $\sigma = IVD_0$ (d).

2.2.4 Simulations

All 3D simulations were performed on a reference volume (V_{ref}) of $1 \times 1 \times 1 \text{ mm}^3$ and the 2D cases consider an area of $1 \times 1 \text{ mm}^2$. The size of the volume elements are $20 \times 20 \times 20 \text{ }\mu\text{m}^3$ and $20 \times 20 \text{ }\mu\text{m}^2$, respectively.

2.2.4.1 Test of the implemented algorithm

As a test of the implemented algorithm, the oxygen distribution around a single linear vessel was simulated using the parallel line vessel architecture. The radial oxygen partial pressure profile together with the maximum diffusion distance was derived.

2.2.4.2 Oxygen distribution for different vascular architectures and vascular fractions

To investigate the influence of the vascular architecture on tissue oxygenation, oxygen distributions were simulated for the three different vascular architectures described in section 2.2.3. For each architecture, vascular fractions of 1%, 4% and 7% were assumed, as these values are representative of values referenced in several studies [42, 8, 62]. Using the same vascular fraction for each of the three architectures means that the reference volume is always supplied by the same amount of blood. In the model, differences in the oxygen distributions therefore originate only from the different vascular architecture. Oxygen histograms were calculated by sampling the calculated oxygen distributions. For the evaluation, the hypoxic fraction (HF) was defined as the fractional volume with an oxygen partial pressure level lower than 5 mmHg, as was done by many other authors [14, 43, 26, 61, 37].

2.2.4.3 Oxygen distributions for different vascular heterogeneities and vascular fractions

Using the parallel line architecture, the impact of vascular heterogeneity was studied using the following distribution of vessels: (i) completely randomly distributed, (ii) partly randomly distributed with $\sigma = IVD_0$, and (iii) partly randomly distributed with $\sigma = IVD_0/4$. For each of the three cases oxygen distributions and histograms were simulated for vascular fractions of 1%, 4% and 7%.

2.2.4.4 Acute hypoxia

So far, only diffusion-limited (chronic) hypoxia was assumed. However, the model can be easily extended to simulate the oxygen distribution in additional presence of ischemic and hypoxemic hypoxia, if suitable input data is available from the patient. Ischemic hypoxia describes reduced oxygen supply due to transient stop of blood flow, e.g. by arterial vasomotion, vascular remodelling or temporary obstruction of vessel lumen by tumour cells, blood cells and/or fibrin aggregates [4]. Hypoxemic hypoxia results from reduced oxygen concentration within the vessels, e.g., by fluctuations in red blood cell flux, transient plasma flow, flow reversal or reduced blood flow [4]. To simulate the additional impact of ischemic hypoxia, 25% of the vessels were randomly selected and inactivated [14]. For the presence of additional hypoxemic hypoxia, in contrast, all vessels remained activated, but the oxygen partial pressure in the vessels was reduced to 75% of the initial value (i.e. 30 instead of 40 mmHg) [43]. This choice is in accordance with published ranges of measured PO₂ fluctuations in tumour vessels [9, 31]. Once again, oxygen distributions and histograms as well as hypoxic fractions were calculated. To get a good visualization of the differences in the oxygen distributions, a vascular fraction of 5% was selected.

2.2.4.5 Conditions of simulation

All simulations were carried out with Matlab R2011b (The Mathworks Inc., MA, USA) on a PC equipped with a 3 GHz Intel® Core™2 Quad processor and 3 GB RAM. An iteration time step of 0.07 s, a kernel width ε of 22 μm (both parameters of the PSE method) and a cutoff for the Verlet lists of 80 μm were used. Calculations of typical 2D and 3D distributions take approximately 20 s and 2 h, respectively.

2.2.5 Comparison of intervessel distances (IVD) distributions with published experimental data

To investigate what degree of heterogeneity is realistic for simulating tumours, a comparison with published experimental *IVD* distributions [34, 33, 22] was performed. For the comparison, artificial vascular fraction values were adjusted such that the resulting simulated mean *IVDs* are the same as in the experimental data. These values were obtained by calculating the mean *IVD* of parallel linear vessels for many different vascular fractions in an area of 12x12 mm². This results in a smooth curve from which the appropriate vascular fraction can be selected.

2.3 Tumour response model (TRM)

2.3.1 Structure of the model

The tumour response model was written in C++ considering the different biological processes shown in the diagram of Figure 2.6. It is based on voxels forming a cubic 3D grid, each of them containing different types of cells: tumour, normal, capillary and dead cells.

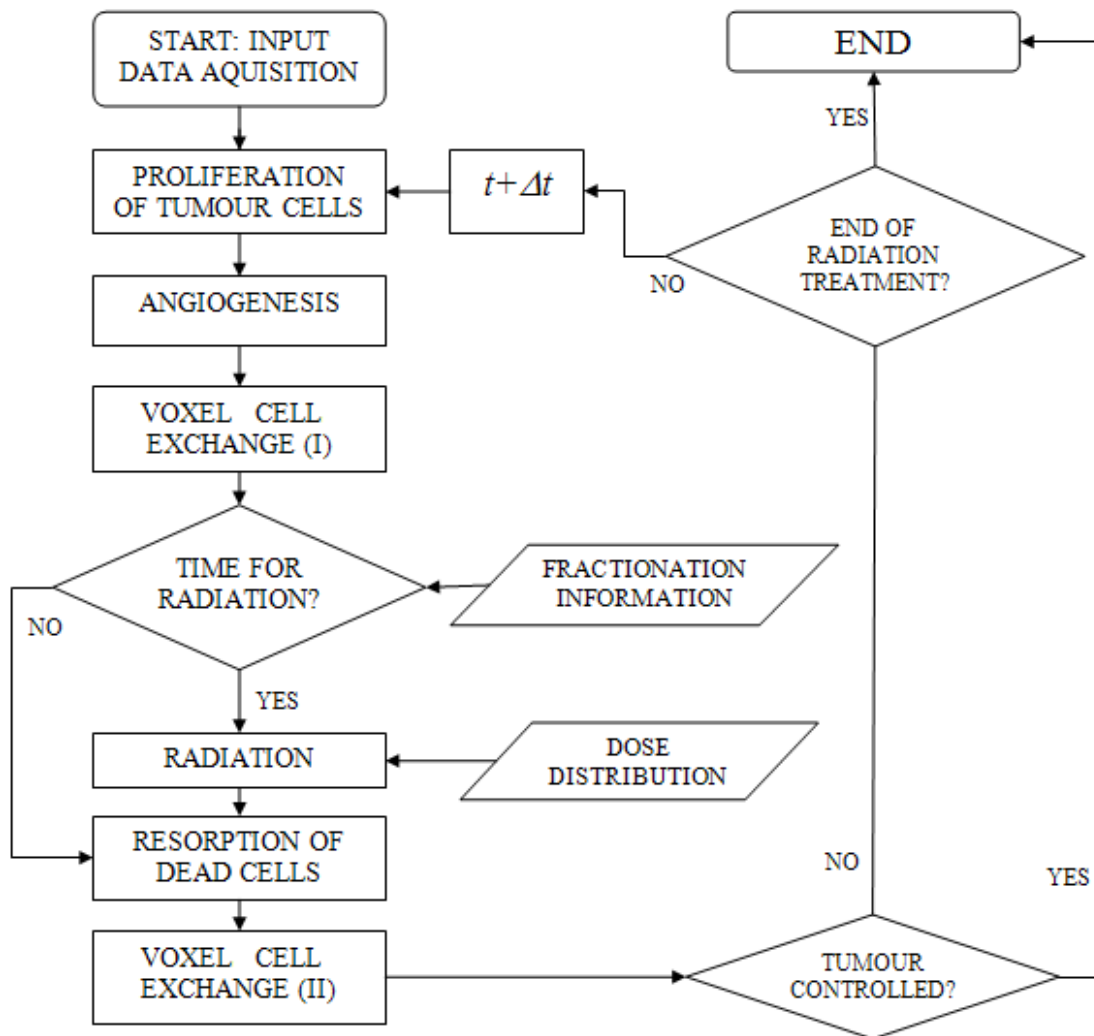


Figure 2.6: Flow chart of the tumour response model.

2.3.1.1 Input data to TRM

The first step in the simulation process is to create a virtual 3D tumour, including as much tumour-specific information as possible, and its surrounding structures, which may be bone, normal soft tissue or air. The model considers four types of input information:

- **Characterization of the tumour prior to irradiation.** Prior to simulating the radiation response, the shape and the biological properties of the tumour have to be characterized. This includes the shape of the tumour, the shape and relative positions of bone, air and normal soft tissue regions, the distribution of vascular fraction as well as the tumour cell density distribution within the tumour.

The information about the shape of the tumour may be taken from the tumour contour delineated in the treatment planning CT. As the voxels of CT images are normally non-cubic, an intermediate step is necessary to interpolate the CT voxels into cubic voxels. Additionally, bone and air regions present in the neighbourhood

of the tumour may also be considered. Voxels that are not tumour, air or bone are considered to be normal soft tissue.

The number of capillary cells per voxel is obtained from a file containing the vascular fraction information for each voxel, which can be in principle obtained from PET [65, 74] and MRI [76] or which can be manually assigned. Some information about the density distribution of tumour cells may be obtained by medical imaging as well, but this is not considered in this work. Therefore the fraction of tumour cells per voxel, as well as that of normal and dead cells (if present) are assigned manually, so that the density of cells is equal to μ all over the tumour (see Table 2.1). A voxel volume of 1.42 mm^3 was used in this work, because a voxel side length of 1.124 mm (corresponding to a typical voxel size length of available CT data) was considered.

- **PO2 histograms.** The model incorporates a database containing simulated oxygenation histograms corresponding to different values of the vascular fraction and a given vascular architecture. These histograms are pre-calculated using the tumour oxygenation model (TOM). For the simulation of the oxygen histograms, a vascular architecture consisting of parallel random distributed vessels (see section 2.2.3.2) was assumed. If dead cells are present in a voxel, the corresponding maximum consumption rate was reduced according to the fraction of viable cells, because dead cells are not supposed to consume oxygen. The database includes histograms for vf in the range 0.1-10.0% in steps of 0.1%, and for fractions of dead cells in the range 0-100% in steps of 10%. As a result, each tumour voxel is always associated with an oxygenation histogram, which depends on the vascular fraction and the fraction of dead cells in this voxel. In this way the heterogeneity of the oxygen distribution is described for each voxel on a microscopic scale. With this approach the experimentally important hypoxic fraction, HF, defined as the fractional volume with an oxygen partial pressure level lower than 5 mmHg, can be calculated for each voxel.
- **Tumour response parameters.** These parameters describe the radiosensitivity, the dynamical behaviour of the tumour and model-specific parameters and are read from a text file that is loaded at the beginning of the simulations. The parameters related to the tumour biology are specified in Table 2.1. Due to the fact that parameter values are normally strongly dependent on tumour type, the values were selected for the special case of a squamous cell carcinoma of the head and neck, which is known to be susceptible for hypoxia. If not specified otherwise, these input data were used throughout this work. The data were taken from different publications, as indicated in the references in parentheses in Table 2.1.

Table 2.1: Biological parameters used for the simulations.

Parameter	Symbol	Value
Cell density	μ	10^6 cells/mm ³ [64]
Tumour cell proliferation doubling time	tp	122.4 h [55]
Angiogenesis proliferation doubling time	ta	612 h (5 times slower than tp . [16])
Half time of dead cell resorption	tr	168 h (1 week) (within the range given by Harting <i>et al.</i> [26])
Radiosensitivity (LQ-model)	α	0.273 Gy ⁻¹ [38]
	β	0.045 Gy ⁻² [38]
Variation of radiosensitivity	σ_α	0,10%
Maximum value of the OER	m	3 [25]
Oxygen partial tension at OER=(m+1)/2	k	3 mmHg [25]

- **Treatment parameters.** Simulation of irradiation is simulated according to the fractionation scheme, which indicates the start of radiotherapy, the number of fractions, and the number of fractions per day as well as the dose per fraction.

The dose at each fraction was assumed to be delivered instantaneously and fractions were separated by one day in the simulations. Consequently, as the full-repair interval takes normally between 6 and 24 hours [64], it was not necessary to consider effects of incomplete repair. In this work five daily 2 Gy fractions per week and no irradiation on weekends were assumed. For simplicity, all simulations started on Mondays.

In addition to the parameters of the fractionation scheme, the spatial dose distribution has to be specified. The model considers the option of incorporating the planned dose distribution. This information is taken from a file containing relative dose values for each voxel. Dose values per voxel can be manually assigned as well. To demonstrate the working of the TRM, dose values were manually assigned in this work.

2.3.1.2 Tumour cell proliferation

To simulate proliferation of tumour cells, the number of tumour cells in each voxel is multiplied by a proliferation factor PF :

$$PF = e^{\left(\frac{\ln(2)}{tp}\right)\Delta t} \quad (2.21)$$

Δt is the simulation time step, whose value is set to 6 hours for all simulations. In principle, the proliferation rate may be assumed to be dependent on the available oxygen and this could easily be implemented. While Nordmark *et al.* [48] report a correlation between short tumour cell doubling time and poor oxygenation, Höckel and Vaupel [27] state that changes in proliferation rates above oxygen partial tensions of 0.2-1 mmHg are negligible. In addition, cells with oxygen levels below this threshold would proliferate more slowly. Due to these uncertainties, no effect of hypoxia on cell proliferation was considered in this model, if not otherwise mentioned.

2.3.1.3 Angiogenesis

Capillary cells are assumed to proliferate, if the hypoxic fraction is different from zero. In this case, the number of capillary cells corresponding to the hypoxic fraction is multiplied by a proliferation factor PF_{angio} , similar to PF of Equation (2.21), but with a larger doubling time (Table 2.1):

$$PF_{angio} = e^{\left(\frac{\ln(2)}{ta}\right)\Delta t} \quad (2.22)$$

2.3.1.4 Cell survival after irradiation

The survival fraction SF of irradiated tumour cells is calculated by the linear quadratic model, modified to consider the dependence on oxygenation status [26] (Equation (2.10)). For each voxel, SF is calculated for each bin of the corresponding oxygenation histogram, where P_{O_2} (used to calculate the OER according to Equation (2.9)) is taken as the central position of each bin. The total number of surviving cells in the voxel is obtained by summing the surviving cells at each oxygenation level. If the number of surviving tumour cells at each oxygenation level is large, the number of surviving cells corresponds simply to the survival fraction SF . If the number of surviving tumour cells is below 10^* , the fate of each tumour cell was determined individually according to the SF , using a random number generator. In this way, stochastic effects occurring for small numbers of cells are considered.

* No difference in the results is seen when using larger threshold values. The value of 10 reflects well the stochastic properties of cell survival and is at the same time computationally efficient.

2.3.1.5 Resorption of dead cells

It is assumed that the resorption of dead cells follows an exponential law. This means that the probability of each dead cell to disappear in every time step of the simulation is:

$$RF = 1 - e^{-\left(\frac{\ln(2)}{\text{tr}}\right)\Delta t} \quad (2.23)$$

For a large amount of dead cells in a voxel, RF indicates the fraction that is resorbed. If less than 10 dead cells remain in a voxel, the same probabilistic approach as described in the previous section is used and RF indicates the probability of each cell to be resorbed.

2.3.1.6 Exchange of cells between voxels

No distribution of cells between voxels takes place if the cell number in each voxel lies in the range corresponding to the density range $\mu \pm 10\%$ *. If the cell numbers in some voxels becomes higher than the upper limit due to proliferation, these voxels transfer cells to their neighbourhood ("Voxel cell exchange (I)" in Figure 2.6), consisting of 26 voxels (Figure 2.7a). Only neighbouring voxels with lower cell densities may receive cells, and the amounts of cells transferred are proportional to the differences of cell numbers between voxels and inversely proportional to the Euclidean distances between their centres (Figure 2.7b). The number of transferred cells per cell type reflect the cell type distribution of the 'donor' voxel, i.e. if 10% of the cells in the 'donor' voxel are capillary cells, 10% of the transferred cells are capillary cells too, and the same occurs for the other cell types (Figure 2.7c). This exchange process is repeated until the cell number of all voxels have arrived in the accepted range. As a consequence, the number of voxels containing tumour cells increase, which leads to tumour growth.

* The choice of an acceptance range is reasonable, because cell number fluctuations are normally present in tumours. The value 10% allows a good performance of the simulation, but choosing another value does not influence the simulation results.

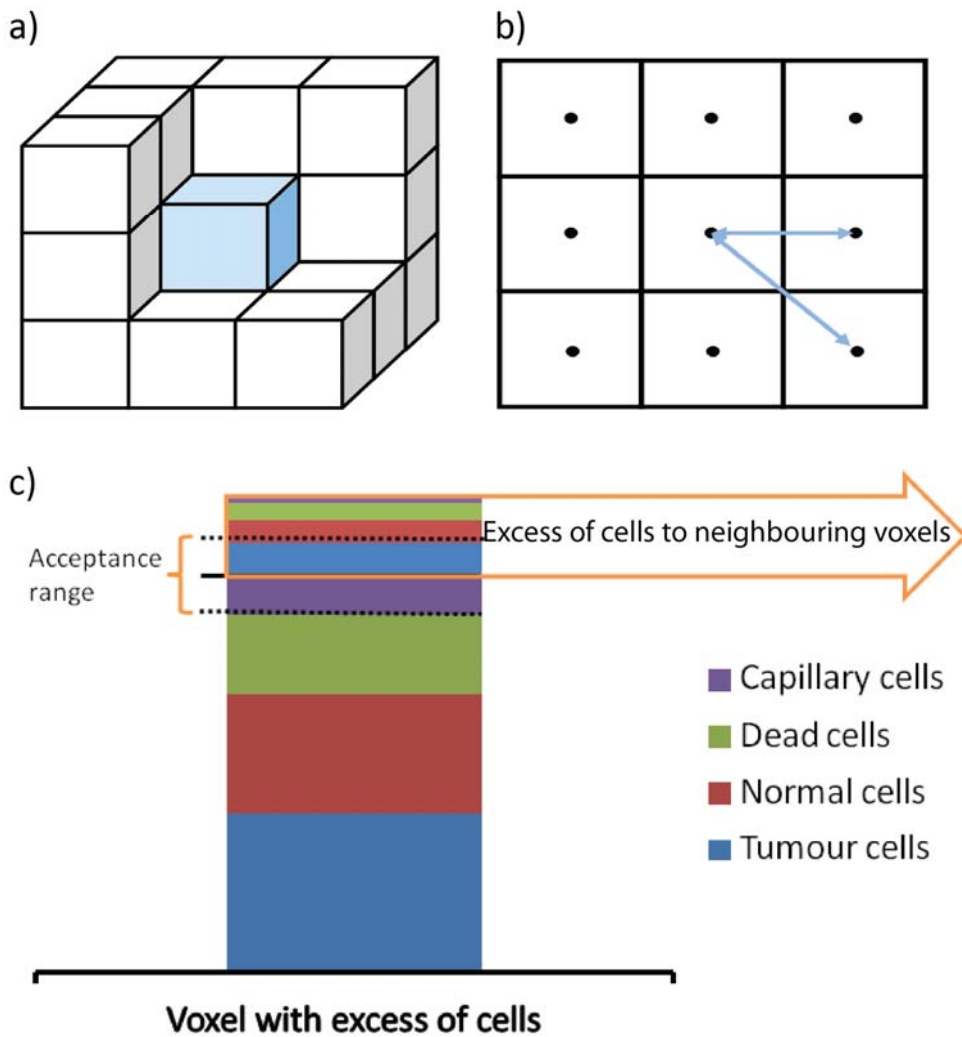


Figure 2.7: a) Representation of a voxel surrounded by some of the 26 neighbouring voxels. b) The distances between voxels are measured from centre to centre, as shown in this 2D representation. c) If a voxel exceeds the upper limit of the acceptance range (upper dotted line), the complete excess of cells is transferred to the neighbouring voxels containing fewer cells. The number of cells received by each of these voxels is inversely proportional to the distance between voxels and proportional to the difference of the cell number of the respective voxels. The fractions of the transferred capillary, normal, dead and tumour cells are the same as in the 'donor' voxel.

On the other hand, if the density in some voxels becomes lower than the lower limit of the acceptance range due to resorption of dead cells, these voxels receive cells from their neighbourhood ("Voxel cell exchange (II)" in Figure 2.6). The process is similar to the one for growth explained previously. In this case, however, the voxels with a too low density receive cells only from the voxels in their neighbourhood that are equally close or closer to the surface of the tumour. This distance is defined as the Euclidean distance between the centres of the corresponding voxel to the centre of the closest non-tumour voxel (Figure 2.8). The process begins with the voxels that are most distant to the tumour border. As a result, the virtual tumour shrinks.

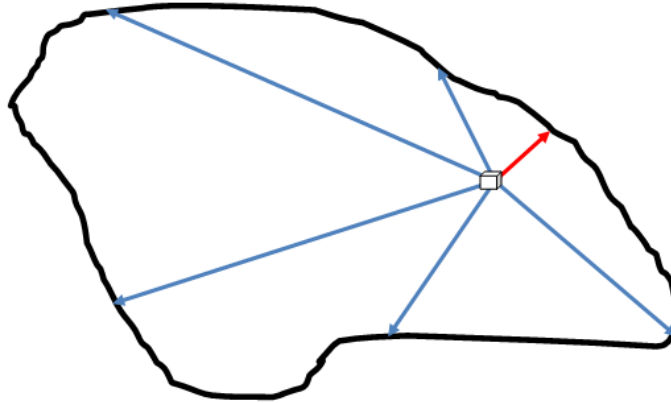


Figure 2.8: 2D representation of a virtual tumour with irregular shape. As an example, the arrows indicate some distances to non-tumour voxels (corresponding to the tumour border) from a selected voxel within the tumour. In the model, the distance from this voxel to the border is defined as the shortest Euclidean distance (displayed in red).

In the model, the transfer of cells to bone voxels is strictly forbidden and the growth into normal soft tissue or air is always allowed. During the shrinkage process, the voxels that loose all tumour cells are assumed to lose the status of tumour voxel and recover their original status, being air or normal soft tissue.

2.3.2 Generation and visualization of the results

In each main iteration step of the simulation, information about the status of the virtual tumour can be stored for later analysis. For example, a map of tumour cell density for any 2D plane in the three orthogonal directions can be saved as a text file. The image processing software Gnuplot (Version 4.2) was used to convert this data into .PNG images, which can also be converted into an .AVI video, if required. Such images or videos may be created also for dead cells, vascular fractions and hypoxic fractions. In all these images, bone and air regions are indicated as an underlying grey image, if present.

To simulate TCP, the response of the virtual tumour to radiotherapy is simulated many times for different dose levels. This is done by means of a script that is able to run many simulations and change the number of fractions in the parameters file. Due to the random nature of the radiation response, some virtual tumours are controlled (i.e. all tumour cells are killed) at a certain dose level, while others remain uncontrolled (i.e. at least one tumour cell survives). The number of controlled tumours, x , and the total number of simulated tumours, n , are stored for each dose level, which allows to calculate the incidence rate x/n . TCP curves are adjusted with software Origin Pro using the logistic dose response model [26]:

$$TCP(D) = \frac{1}{1 + e^{-b_0 - b_1 D}} \quad (2.24)$$

where D is the total dose and b_0 and b_1 are the fitting parameter. The tolerance dose TD_{50} (the dose at 50% TCP) is then given by

$$TD_{50} = -\frac{b_0}{b_1} \quad (2.25)$$

2.3.3 Simulations

Although the model is able to use input information obtained from medical imaging techniques, no patient-specific input data was considered in this work. Rather, artificially created virtual tumours with simple geometries are used as this allows more systematic evaluations and comparisons of the influence of the different model components. In addition, all simulations consider the same bone, soft tissue and air regions (as indicated in Figure 2.9).

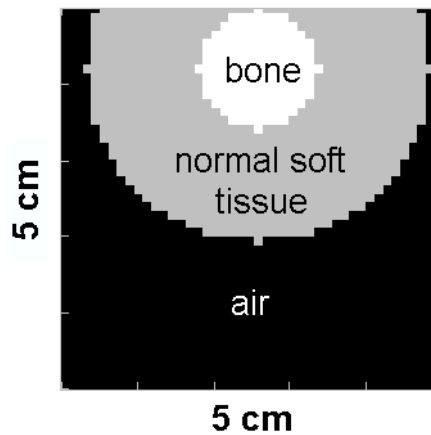


Figure 2.9: Bone, air and normal soft tissue regions. This $5 \times 5 \text{ cm}^2$ region is part of one of the equal slices that make up the simulation volume. The geometry is thus axisymmetric.

2.3.3.1 Tumour growth

Tumour growth is simulated by beginning with a single tumour voxel, containing tumour and capillary cells, assuming the parameters values of Table 2.1. Specifying a certain vascular fraction in this voxel (and in the surrounding normal tissue), the growth is simulated until the tumour reaches a diameter of approximately 3 cm. To obtain a median hypoxic fraction of 38%, as measured with Eppendorf electrodes in head and neck squamous cell carcinomas (SCCs) by Nordsmark *et al.* [47], a vascular fraction of 3.6% was chosen, which is a realistic value. As no dead and normal cells are considered in this single initial voxel, the remaining cells (96.4%) are assumed to be tumour cells. At every time point during the simulations, the distributions of tumour cells and vascular fraction of a central tumour slice are saved.

To evaluate the impact of angiogenesis and proliferation of tumour cells on tumour properties, two additional studies were performed:

- **Impact of angiogenesis during tumour growth.**

To study the effect of angiogenesis during tumour growth, two additional simulations were performed, beginning again with one single tumour voxel: in the first simulation, angiogenesis was inactivated while in the second, the proliferation rate of capillary cells due to angiogenesis was increased by a factor 5 to consider a case in which capillary cells proliferate at the same rate as tumour cells.

- **Impact of changing the proliferation rate during tumour growth.**

In addition, the impact of a modified proliferation rate of tumour cells was studied. Two additional values of tp were considered: 30.6 h and 489.6 h, corresponding to one fourth and four times the value previously used (Table 2.1). These values lie within the range of values published by Price *et al.* [55] for squamous cell carcinomas of the head and neck.

2.3.3.2 *Tumour shrinkage during radiotherapy*

The response to radiotherapy of a virtual tumour of approximately 3 cm in diameter is simulated using a standard fractionation regime: 2 Gy per fraction (uniformly distributed over the tumour), 5 fractions per week over 6 weeks. For the initial distribution of tumour cells and vascular fraction, the state obtained at the end of the growth simulation described in section 2.3.3.1. was used as starting condition to consider a virtual tumour of approximately 3 cm of diameter and a median hypoxic fraction of 38%, as indicated by Nordmark *et al.* [47] for head and neck SCCs. At every time point during the simulations, the distributions of tumour cells and vascular fraction of a central tumour slice were saved.

During radiotherapy, hypoxic tumours may reoxygenate. Within the presented model, there are three different mechanisms which may contribute to reoxygenation of the tumour:

- (1) Angiogenesis.
- (2) Decrease of the maximum average oxygen consumption rate of cells due to higher fraction of dead cells, which do not consume oxygen.
- (3) Transport of capillary cells from the tumour periphery towards tumour core due to tumour shrinkage.

To study the impact of these three mechanisms on reoxygenation, the simulation of tumour response to irradiation of the previous section was repeated three times by

inactivating two of the three mechanisms. For example, to consider only angiogenesis, the mechanisms 2 and 3 are inactivated. Angiogenesis (1) was inactivated directly in the code. The decrease of the oxygen consumption rate due to dead cells (2) was inactivated directly in the model for the oxygen consumption. The transport of cells due to tumour shrinkage (3) was inactivated by switching off the resorption of dead cells. In this case no tumour shrinkage and accordingly no transfer of capillary cells occurs.

In addition, the impact of separately changing some model parameters or features during radiotherapy was studied:

- **Impact of angiogenesis**

The impact of angiogenesis is studied by (a) first inactivating angiogenesis and (b) setting the proliferation rate of capillary cells equal to the proliferation rate of tumour cells.

- **Impact of tumour cell proliferation**

As in the previous section, two alternative values of tp are considered: (a) 30.6 h and (b) 489.6 h, corresponding to one fourth and four times the value previously used.

- **Impact of the resorption rate of dead cells**

For this, the half time of the resorption of dead cells was varied. Values of (a) 0.5 weeks and (b) 2 weeks (half and two time the value used in 2.3.3.1) were used. These values lie in the range given by Harting *et al.* [26].

2.3.3.3 Tumour control probability

TCP curves were generated by simulating the tumour response to radiotherapy for many tumours as described in section 2.3.3.2 (using the parameters values of Table 2.1 and an initial mean hypoxic fraction of 38%). Ten tumours were simulated for each dose level, which results in incidence rates between 0% and 100%. Inter-tumour variation of radiosensitivity was considered by varying the value of α . In each simulation, α takes the value obtained by sampling a random variable that follows a normal distributions $N(0.273, 0.0273)$, corresponding to $\sigma_\alpha = 0.1\alpha$. Negative values of α are very unlikely and were disregarded, if they occurred.

The effect of oxygenation on the TCP-curve was studied by comparing the response of this tumour with that of a second tumour, which was assumed to be better oxygenated. For the better oxygenated tumour, a median hypoxic fraction of only 2.4% was used. The initial state of this second tumour (also having a diameter of 3 cm) was also obtained by simulating the tumour growth starting with a single tumour voxel. In this case, the

vascular fraction of this initial voxel (and the surrounding normal tissue) was of 7.2%, which is twice as large as the previously used 3.6%. For this tumour, the TCP-curve was calculated in the same way as described in the previous paragraph.

2.3.3.4 Restricted proliferation of very hypoxic tumour cells

The effect of a potentially restricted proliferation capacity of very hypoxic cells during growth and shrinkage, as discussed by Hockel and Vaupel [27], was studied by allowing the proliferation of only 1/3 or 2/3 of the tumour cells that correspond to the first bin of the oxygen histograms (<2.5 mmHg).

2.3.3.5 Redistribution of dose

Finally, the effect on TCP from redistributing the dose to the tumour, according to the initial distribution of the vascular fraction, was studied using a simplified approach. An integrated dose boost was considered for the central hypoxic region of the same virtual tumour simulated in the previous sections. The tumour core (having half the total tumour volume) receives an increased dose of $2 \text{ Gy} + \Delta d$, while the dose in the periphery (corresponding to the other half of the total tumour volume) receives a reduced dose of $2 \text{ Gy} - \Delta d$. As a result, the integral dose and hence the total energy delivered to the tumour is conserved and only a redistribution of dose takes place. Δd was chosen such that the survival fraction in the hypoxic tumour centre is equal to the survival fraction at the tumour periphery.

3 Results

3.1 Tumour oxygenation model (TOM)

3.1.1 Test of the implemented algorithm

An oxygen partial pressure profile simulated for a single vessel is shown in Figure 3.1. The maximum oxygen diffusion distance of approximately 150 μm is comparable with published values [68, 49, 14].

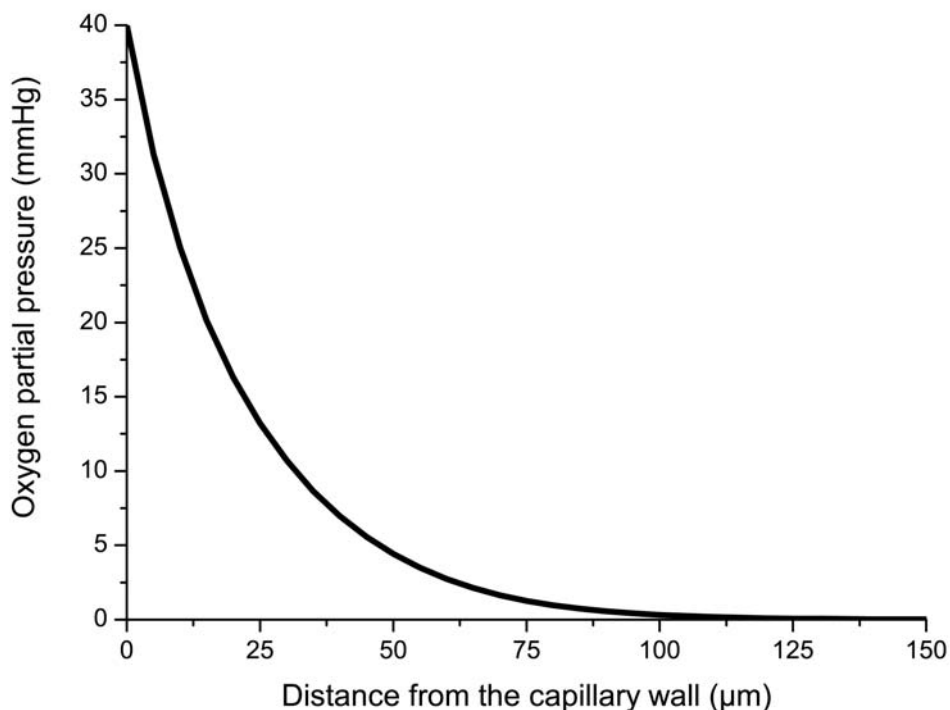


Figure 3.1: Oxygen partial pressure radial profile around a single vessel using the parallel linear vessel architecture.

3.1.2 Oxygen distribution for different vascular architectures and vascular fractions

In Figure 3.2 the oxygen distributions and the corresponding histograms for the combinations of the three different vascular architectures and three selected vascular fractions are shown. As expected, the hypoxic fraction decreases and the histograms are shifted to higher oxygen values with increasing vascular fraction for all three architectures indicating an improved oxygen supply. While for $vf = 1\%$, the histograms for the point-like and parallel linear architecture are relatively similar, a marked difference can be seen for higher vascular fractions. At $vf = 4\%$ and 7% , the width of the oxygen histogram for the

point-like architecture is substantially smaller and shows no hypoxic fraction at all. This indicates that the point-like architecture leads to much more homogeneous oxygen distributions than the parallel line architecture. In contrast, although the 2D-distributions of the parallel line and the 3D linear vessel architecture suggest a difference in oxygenation, there are no noticeable differences in the oxygen histograms ($p > 0.79$ in all cases, two-tailed Mann-Whitney U test). This indicates that the 2D and 3D parallel line architectures lead to a comparable oxygen supply.

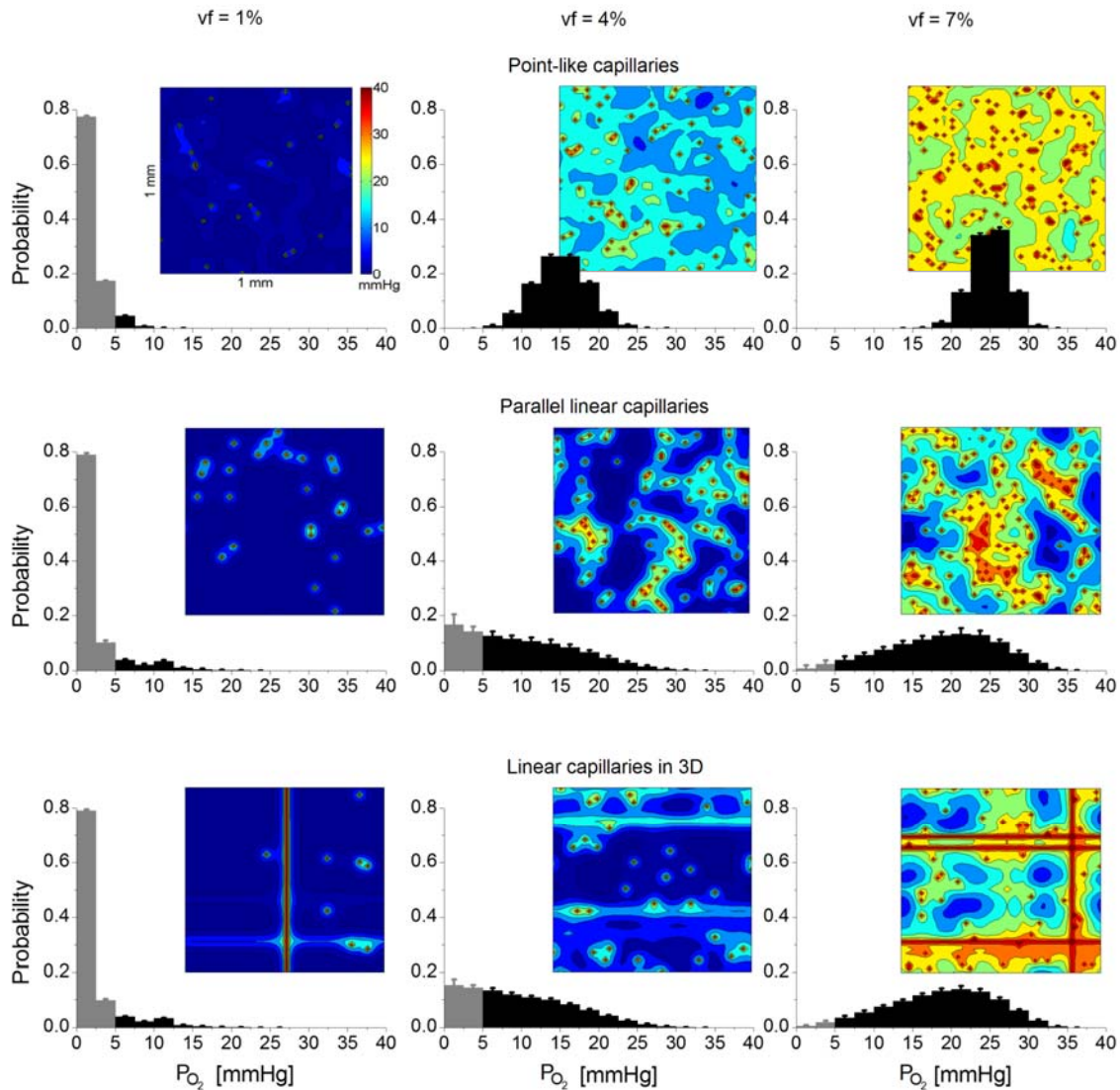


Figure 3.2: Simulated oxygen distributions and histograms for different vascular architectures (top: point-like vessels; middle: parallel linear vessels; bottom: linear vessels in 3D) and vascular fractions (1%, 4% and 7%, from left to right). The 2D oxygenation maps have an area of $1 \times 1 \text{ mm}^2$ and the coloured scale ranges from 0 to 40 mmHg, as indicated in the upper left figure. The grey bins in the histograms mark the hypoxic fraction. Note: For visualization, representative images of the oxygen distribution were selected. Error bars of the bins of the histograms indicate the standard deviation of repeated simulations ($n=20$).

3.1.3 Oxygen distributions for different vascular heterogeneities and vascular fractions

Figure 3.3 shows the oxygen histograms for the parallel line architecture assuming different heterogeneities and different vascular fractions. It can be seen that the complete and the partial random distribution of the vessels result in the same distribution if the heterogeneity parameter σ of the latter is selected equal to IVD_0 . If σ is decreased to $IVD_0/4$, however, a marked difference is seen for vascular fractions of 4% and 7%. For these cases the width of the histograms is considerably reduced. For $vf = 4\%$, this leads also to a markedly reduced hypoxic fraction.

As the differences in the oxygen histograms produced by different degrees of vascular heterogeneity (Figure 3.3) are most likely produced by changes of the intervessel distance distribution, the corresponding distributions were calculated. As can be seen in Figure 3.4, there is no difference between the complete random distribution of vessels and the partial random distribution with $\sigma = IVD_0$ while the distributions for the partial random distribution with $\sigma = IVD_0/4$ is shifted substantially to higher values.

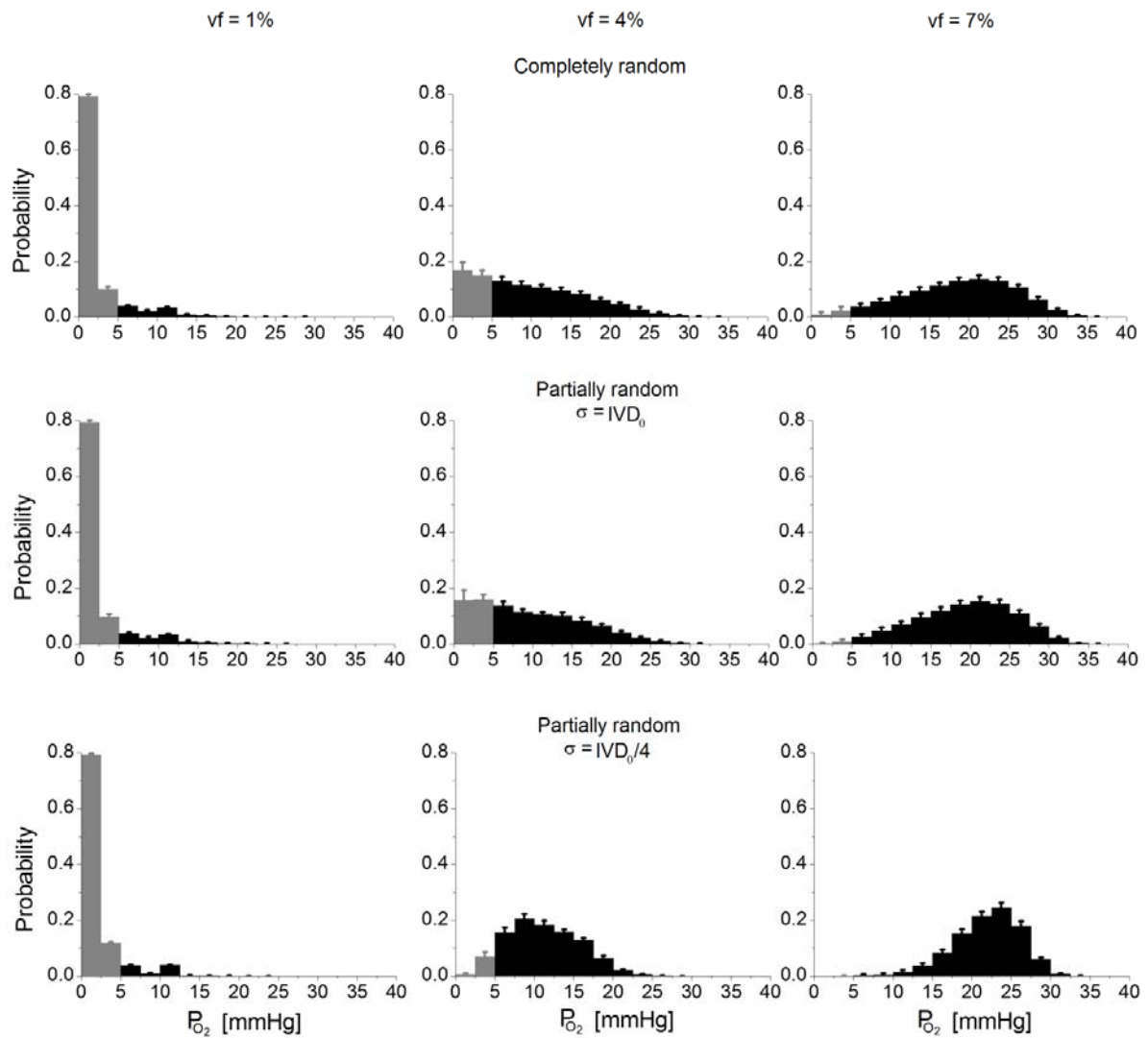


Figure 3.3: Simulated oxygenation histograms for the parallel line architectures of different heterogeneity (top: completely random; middle: partially random with $\sigma = IVD_0$; bottom: partially random with $\sigma = IVD_0/4$) and different vascular fractions (1%, 4% and 7% from left to right). The grey bins in the histograms mark the hypoxic fraction. Error bars indicate the standard deviation of repeated simulations ($n=20$).

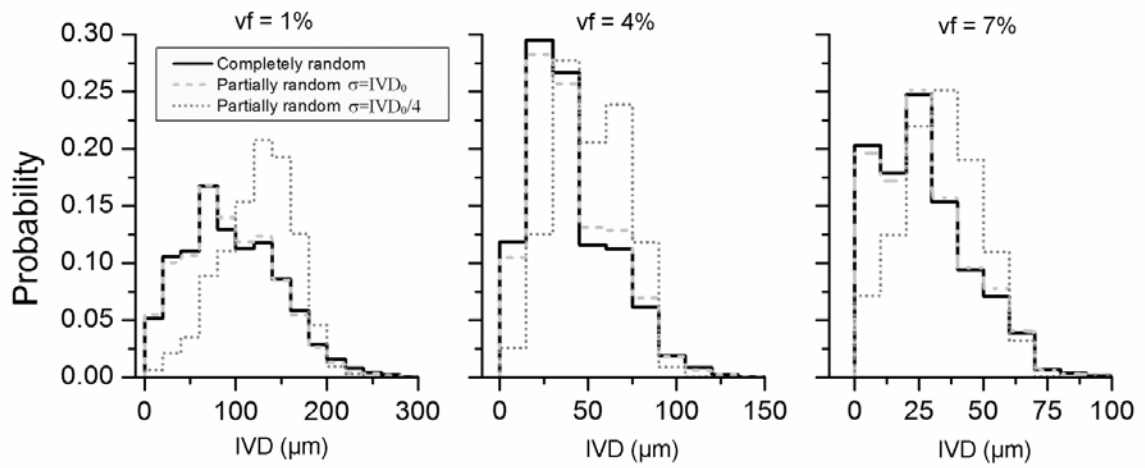


Figure 3.4: Intervessel distance distributions for the parallel line architecture assuming different heterogeneities (completely random and partially random distributed with $\sigma = IVD_0$ and $IVD_0/4$, respectively) and vascular fractions (1%, 4% and 7% from left to right) for the vessels distribution. To increase statistics, a larger reference volume of $12 \times 12 \text{ mm}^2$ instead of $1 \times 1 \text{ mm}^2$ was used for the simulation.

3.1.4 Acute hypoxia

Figure 3.5 shows oxygen distributions and histograms for the presence of chronic hypoxia alone as well as the additional influence of acute hypoxia for a vascular fraction of 5% using the parallel line architecture. Compared to chronic hypoxia alone, ischemic hypoxia leads to a shift of the histogram to lower values and an increased hypoxic fraction. For hypoxemic hypoxia the influence is similar. In this case, oxygen partial pressures larger than 30 mmHg are not allowed according to the assumption, leading to a somewhat narrower histogram.

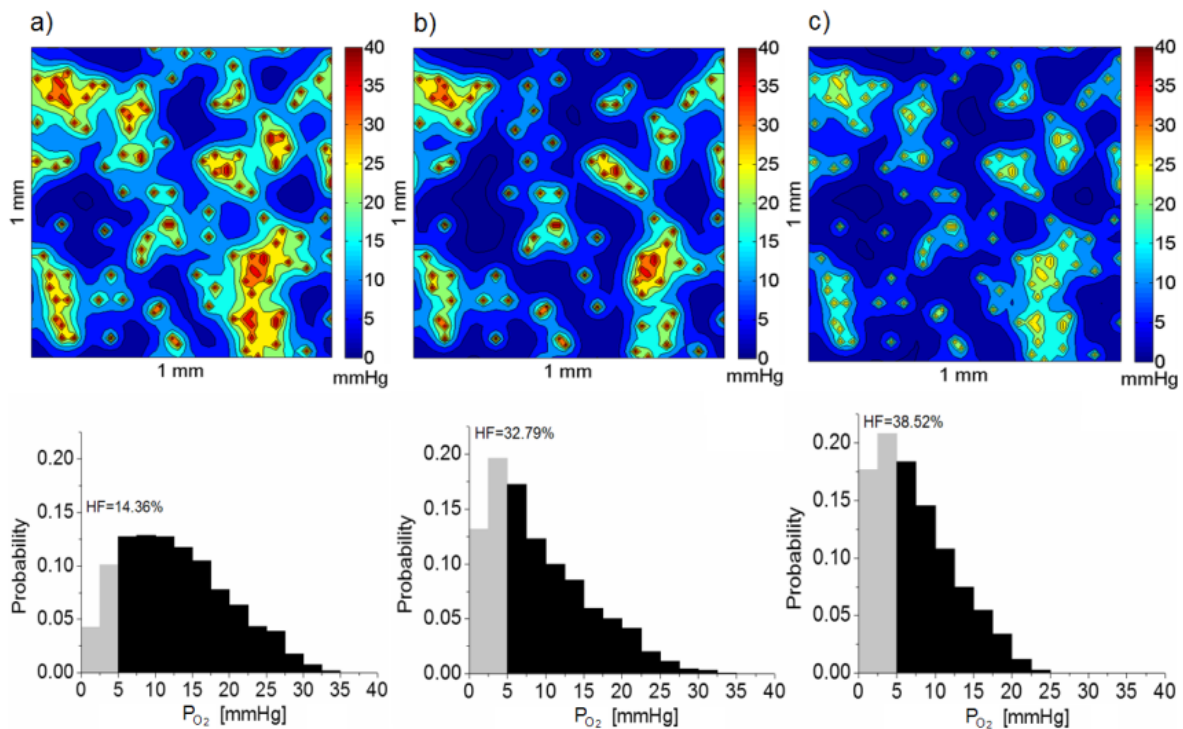


Figure 3.5: Simulated oxygenation maps and histograms for different types of hypoxia: chronic hypoxia alone (left), and additional impact of ischemic hypoxia (middle), and hypoxemic hypoxia (right). The grey bins in the histograms mark the hypoxic fraction (HF). Note: For all three cases the same vessel distribution was assumed.

3.1.5 Comparison of IVD distributions with experimental data

Figure 3.6 shows a representative example, where the simulated IVD distribution is compared with published experimental data. The more heterogeneity was introduced in the simulated vessel distributions, the more similar are the simulated and experimental curves. Using the completely random approach as described in section 2.2.3.2 was found to be most adequate for the simulation of tumours.

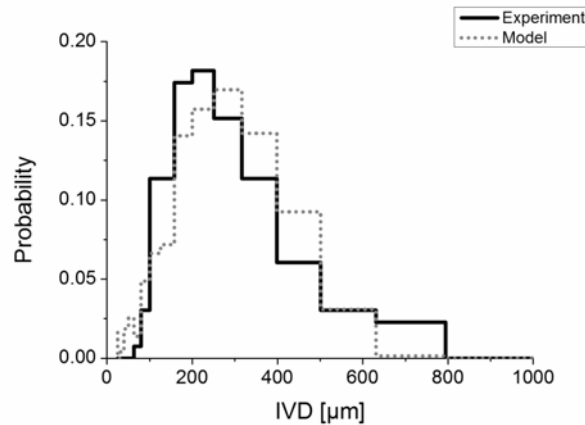


Figure 3.6: The solid line shows the measured IVD distribution of a murine carcinoma (data points taken from Konerding et al. 1999) while the dotted line represents the IVD distribution generated by our model for the same mean IVD (corresponding to a vascular fraction of 0.2%) and using the completely random approach to define the heterogeneity.

3.2 Tumour response model (TRM)

3.2.1 Tumour growth

Figure 3.7 shows the growth of a virtual tumour at five time points, starting from a single voxel with a vascular fraction of 3.6%. The figure shows the distribution of tumour cell density and vascular fraction on a central tumour slice. The tumour grows into soft tissue and air while it cannot invade into the bone. During the growth process, the tumour periphery receives a lower tumour cell density and higher vascular fraction values than the core of the tumour. The appearance of a hypoxic tumour centre is clearly visible.

In Figure 3.8 the impact of angiogenesis is shown. a) and b) refer to the tumour shown in Figure 3.7, which was used as a reference. In c) and d) angiogenesis was inactivated and in e) and f) the proliferation rate for capillary cells was set to the value of tumour cells. No noticeable impact on the distribution of tumour cells can be seen and changes of only a few permille is obtained for the vascular fraction.

In Figure 3.9 the impact of changing the proliferation rate by a factor of 4 is shown. These changes in the proliferation rate lead to substantial changes in tumour growth. While c) and d) show a noticeable smaller tumour (approximately a factor 4 smaller) as compared to the reference tumour shown in a) and b), e) and f) shows an extremely fast-growing tumour (the diameter at $t=300$ h is equal to the diameter at $t=1200$ h in the reference case). For the increased proliferation rate, the simulation was restricted to $t=300$ h, because after this time the tumour became bigger than the simulation region. It should be mentioned that while in b) the vascular fraction of the tumour centre increased with time, it decreases with time, if the proliferation rate is smaller (d). In addition, f) and b)

correspond to tumours of similar sizes but the red curve in f) ($t=300$ h) indicates lower v_f values than the green curve in b) ($t=1200$ h).

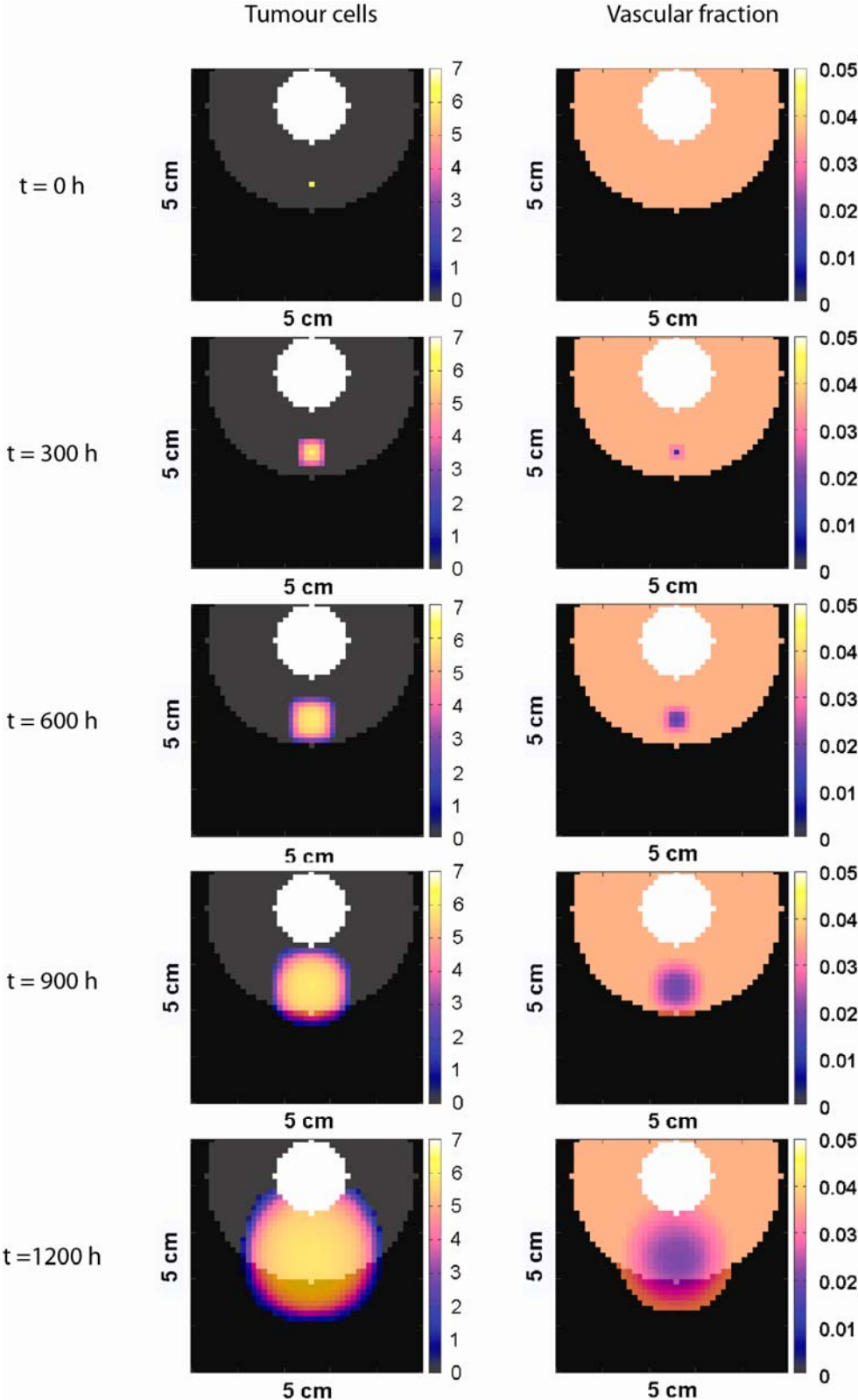


Figure 3.7: Central slices of the simulated tumour growth showing tumour cell density (left, in a logarithmic scale from 10^0 to 10^7) and vascular fraction (right). Anatomy is underplayed in grey (bone: white, soft tissue: grey and air: black, see Figure 2.9 for details).

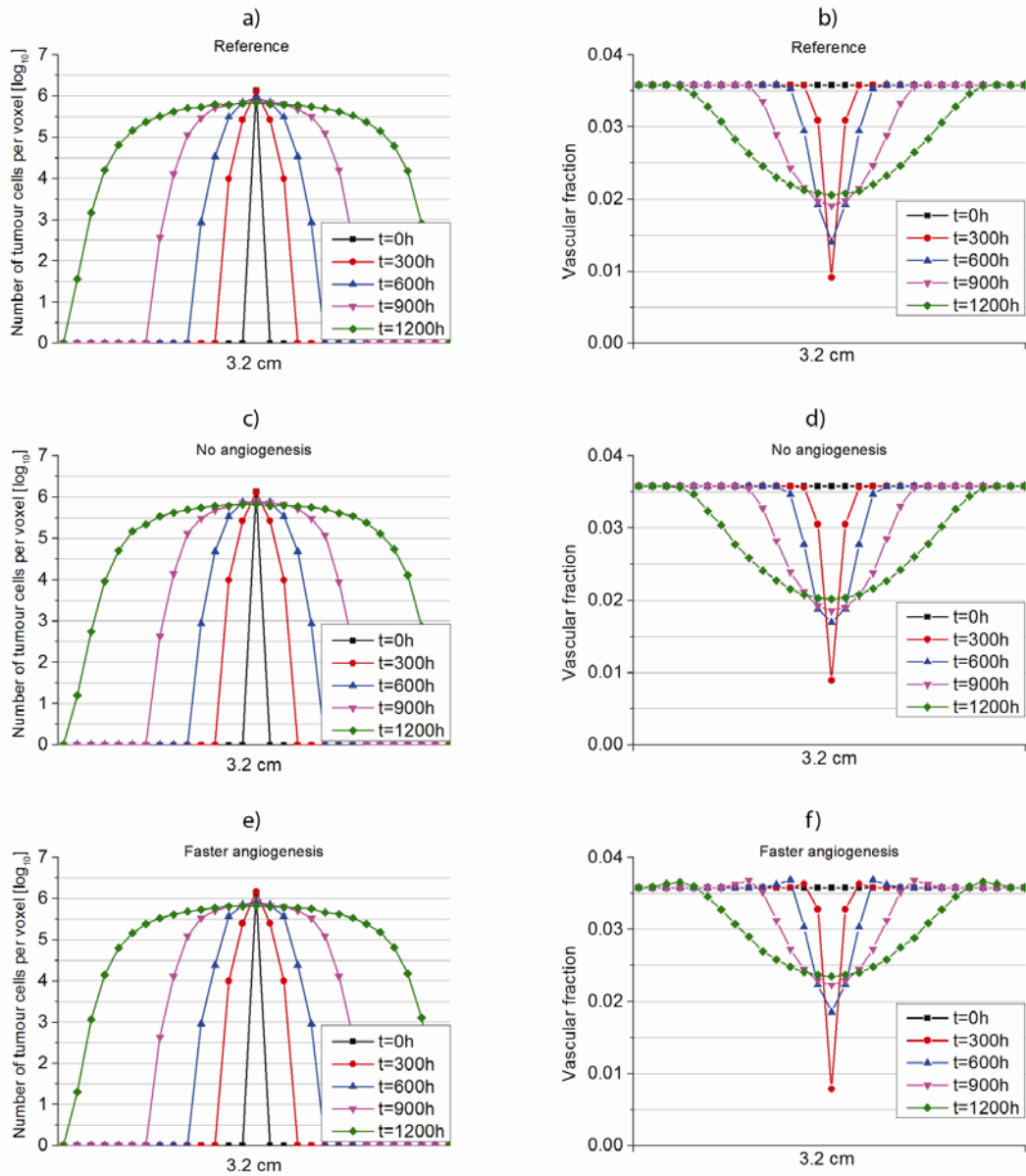


Figure 3.8: Profiles of tumour cell density (left) and vascular fraction (right) on a line through the virtual tumour through its centre while growing. The impact of deactivating angiogenesis (c and d) and considering a faster angiogenesis (e and f) is negligible. The x-axis length, used here and in following figures, is 3.2 cm, for a proper visualization of the simulated tumour of approximately 3 cm in diameter.

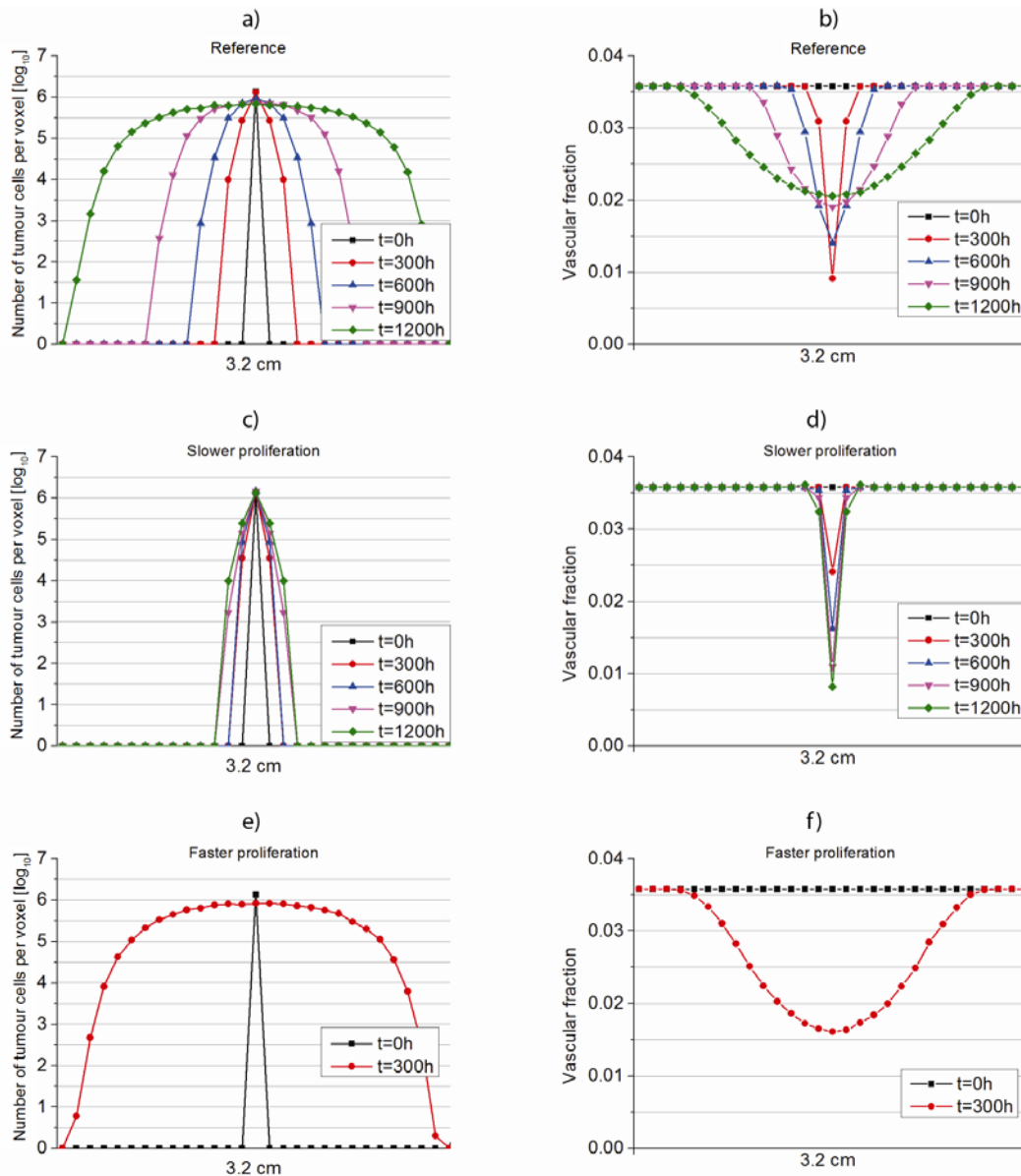


Figure 3.9: Profiles of tumour cell density (left) and vascular fraction (right) on a line through the centre of the virtual tumour while growing. The impact of considering slower (c and d) and faster (e and f) proliferation of tumour cells is shown.

3.2.2 Tumour shrinkage during radiotherapy

Figure 3.10 shows tumour shrinkage during radiotherapy at 5 different time points. The accumulated dose is indicated in the left column. As a starting point for radiotherapy the reference tumour of Figure 3.7 (at $t=1200$) was used. After start of radiotherapy, the virtual tumour of approximately 3 cm diameter starts shrinking and the tumour cell density decreases from approximately 10^6 tumour cells per voxel in the tumour centre to less than 100 at the end of the treatment. At the same time an increase in the vascular

fraction in the centre is observed, from values of about 2% to almost 4% at the end of radiotherapy.

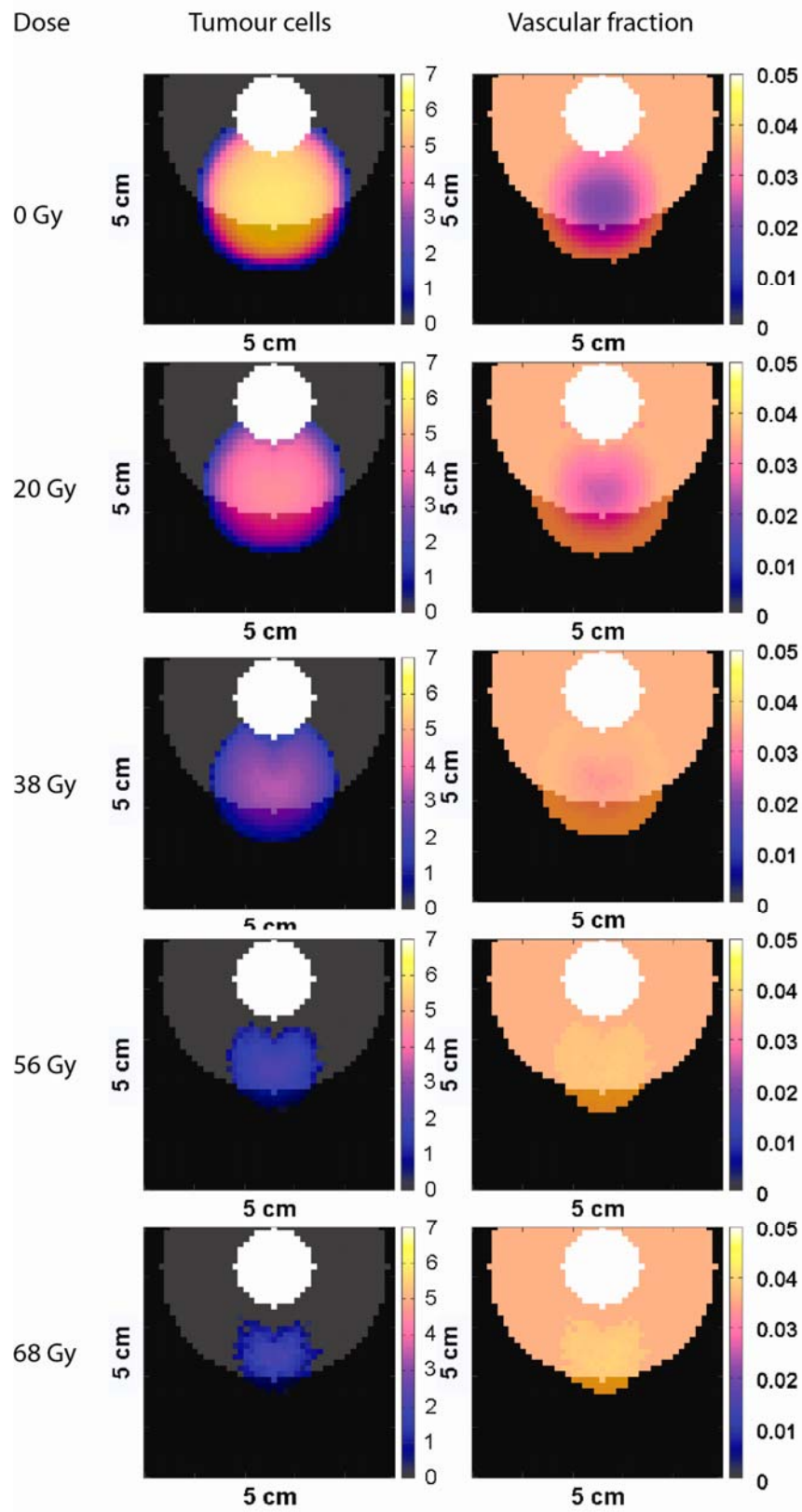


Figure 3.10: Central slices showing tumour cell density (left, in a logarithmic scale from 10^0 to 10^7) and vascular fraction (right) of the simulated tumour shrinkage during radiotherapy.

To investigate the processes leading to reoxygenation, the temporal development of the vascular fraction as well as that of the oxygen distribution was investigated using the tumour displayed in Figure 3.10. For this, the three reoxygenation mechanisms described in section 2.3.3.2 were analyzed separately.

Figure 3.11a shows the vascular fraction profiles through the centre of the tumour displayed in Figure 3.10. This profile includes the sum of the three effects which may lead to reoxygenation of the tumours during radiotherapy. In the other three parts of Figure 3.11 the impact of these three effects on vascular fraction is shown separately. In Figure 3.11b, only the influence of angiogenesis is shown: After an initial decrease of the vascular, the vascular fraction increases slowly during the radiotherapy course. Figure 3.11c shows a similar initial decrease in case of considering the reduced oxygen consumption due to the presence of dead cells, however, no noticeable differences in vascular fraction occurred thereafter. The initial decreases in b) and c) occur because of the proliferation of tumour cells and the absence of resorption of killed cells. Figure 3.11d is very similar to Figure 3.11a and shows that the increase of vascular fraction originates to a great extent from tumour shrinkage. The corresponding PO₂ histograms are shown in Figure 3.12.

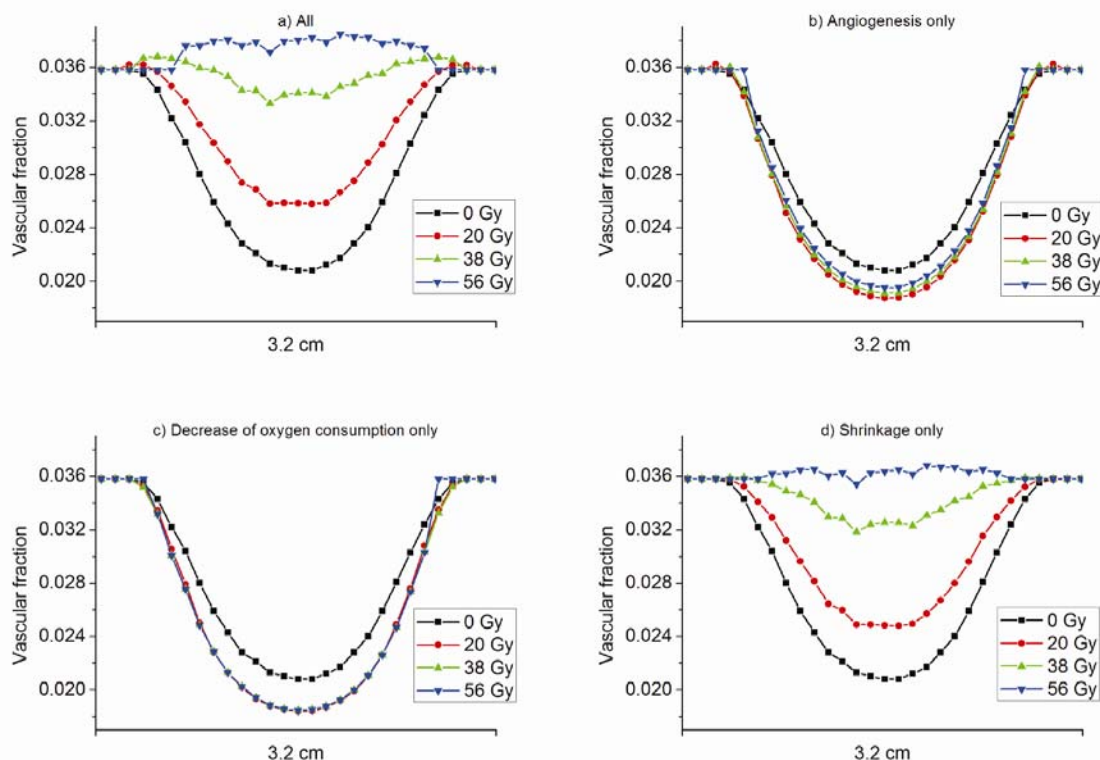


Figure 3.11: Impact on the vascular fraction resulting from the three different mechanisms that contribute to the reoxygenation during radiotherapy: a) sum of the three effects, b) angiogenesis only, c) decreased oxygen consumption due to dead cells only, and d) tumour shrinkage only.

In column a) of Figure 3.12, it can be seen that a major reoxygenation is completed before $t=300$ h, while thereafter only minor changes are observed. A very similar effect is seen in case of tumour shrinkage only (column d), however with slightly higher hypoxic fraction values. The other two effects (columns b and c) show only a very slight changes of the hypoxic fraction, which also takes place before $t=300$ h. Beyond $t=300$ h, no significant changes occur in column c) and in column b). Only a very slight decrease of the hypoxic fraction is observed at $t=900$ h in column b).

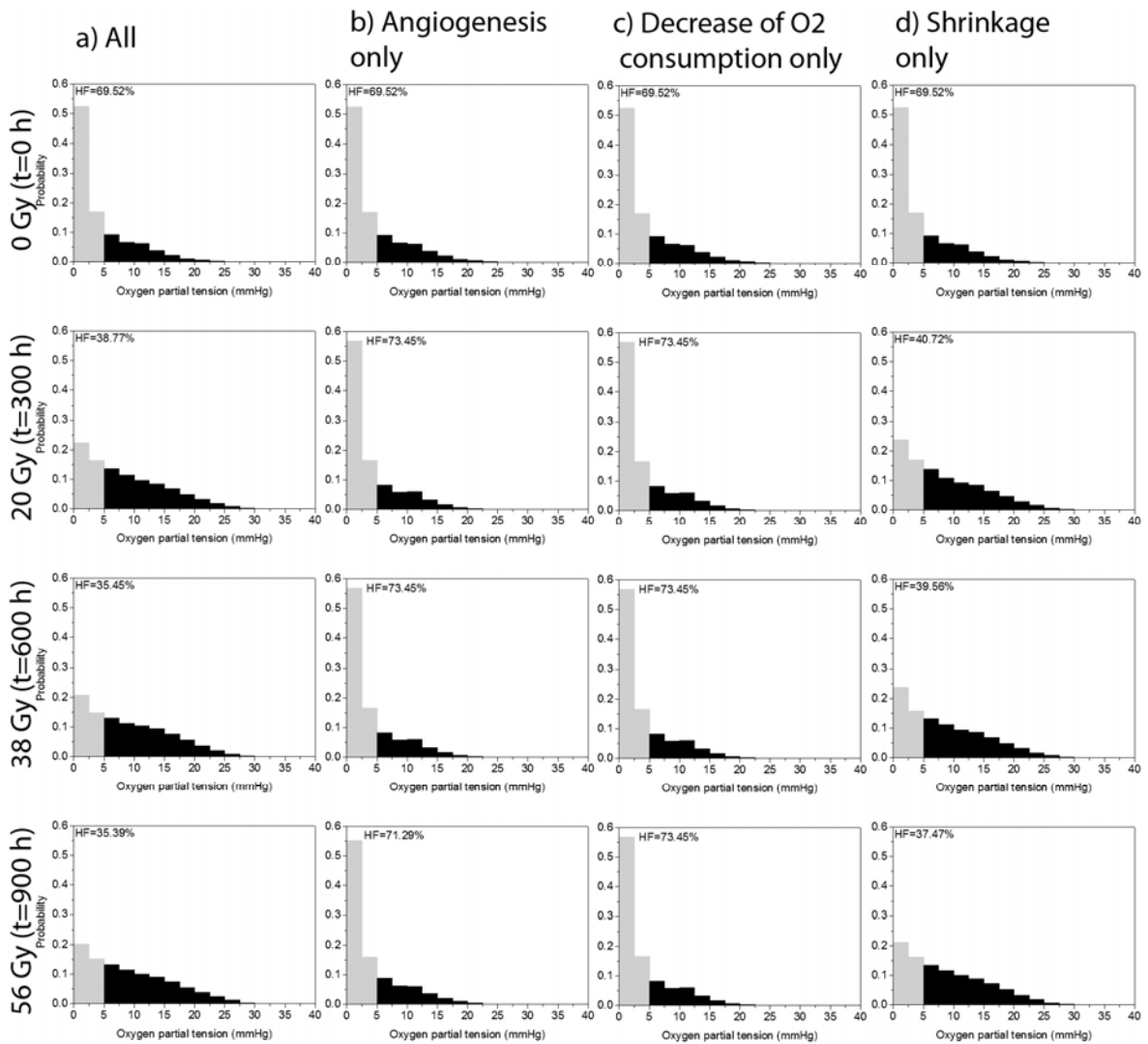


Figure 3.12: Impact of the three different mechanisms that contribute to the reoxygenation during radiotherapy on the microscopic tumour oxygen distribution (PO₂ histograms). a) sum of the three effects, b) angiogenesis only, c) decreased oxygen consumption due to dead cells only, and d) tumour shrinkage only.

Figure 3.13 shows the impact of angiogenesis on tumour cell density and vascular fraction during the radiation treatment. Inactivating angiogenesis leads to a slight reduction of vascular fraction (d) while setting the proliferation rate of capillary cells to that of tumour cells (f) has substantial impact on vascular fraction. In both cases, only slight changes in

the distribution of tumour cells are observed (c and e). In c) a small but noticeable increase in tumour size is seen.

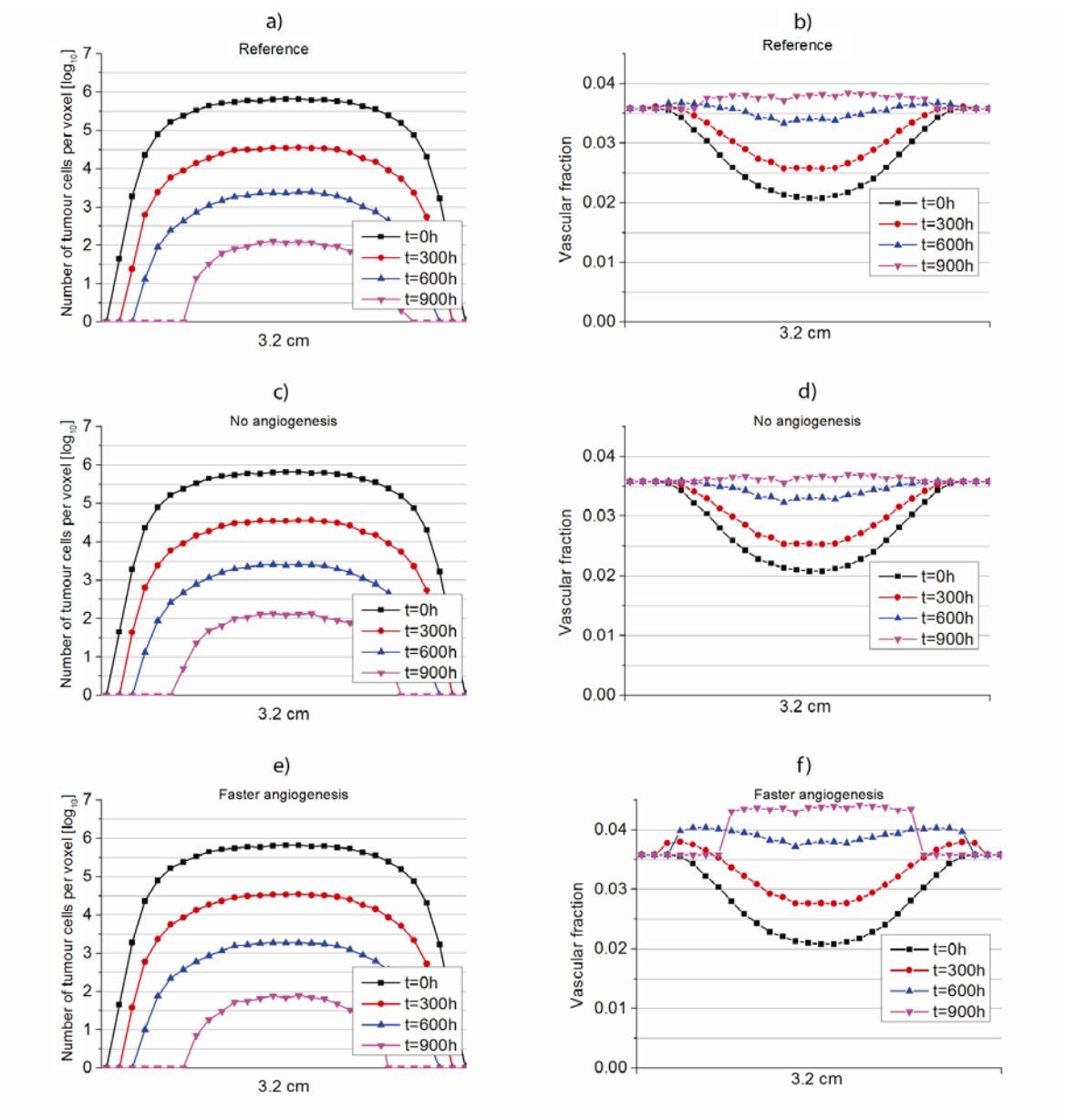


Figure 3.13: Profiles of tumour cell density (left) and vascular fraction (right) on a line through the centre of the virtual tumour during radiotherapy. The impact of deactivating angiogenesis (c and d) and considering a faster angiogenesis (e and f) is shown.

Figure 3.14 shows that the dependence of tumour cell density and vascular fraction on the proliferation rate is high. In these cases the proliferation rate of the reference case was scaled by the factors $\frac{1}{4}$ and 4. In c) one can see that the shrinkage occurs substantially faster and tumour control is achieved before $t=900$ h. In e) only $t=0$ h and $t=300$ h are shown because the virtual tumour grew so fast that it exceeded the displayed field of view already after $t=300$ h. With respect to the vascular fraction, the faster the proliferation, the lower is the vascular fraction in the centre of the tumour and vice versa.

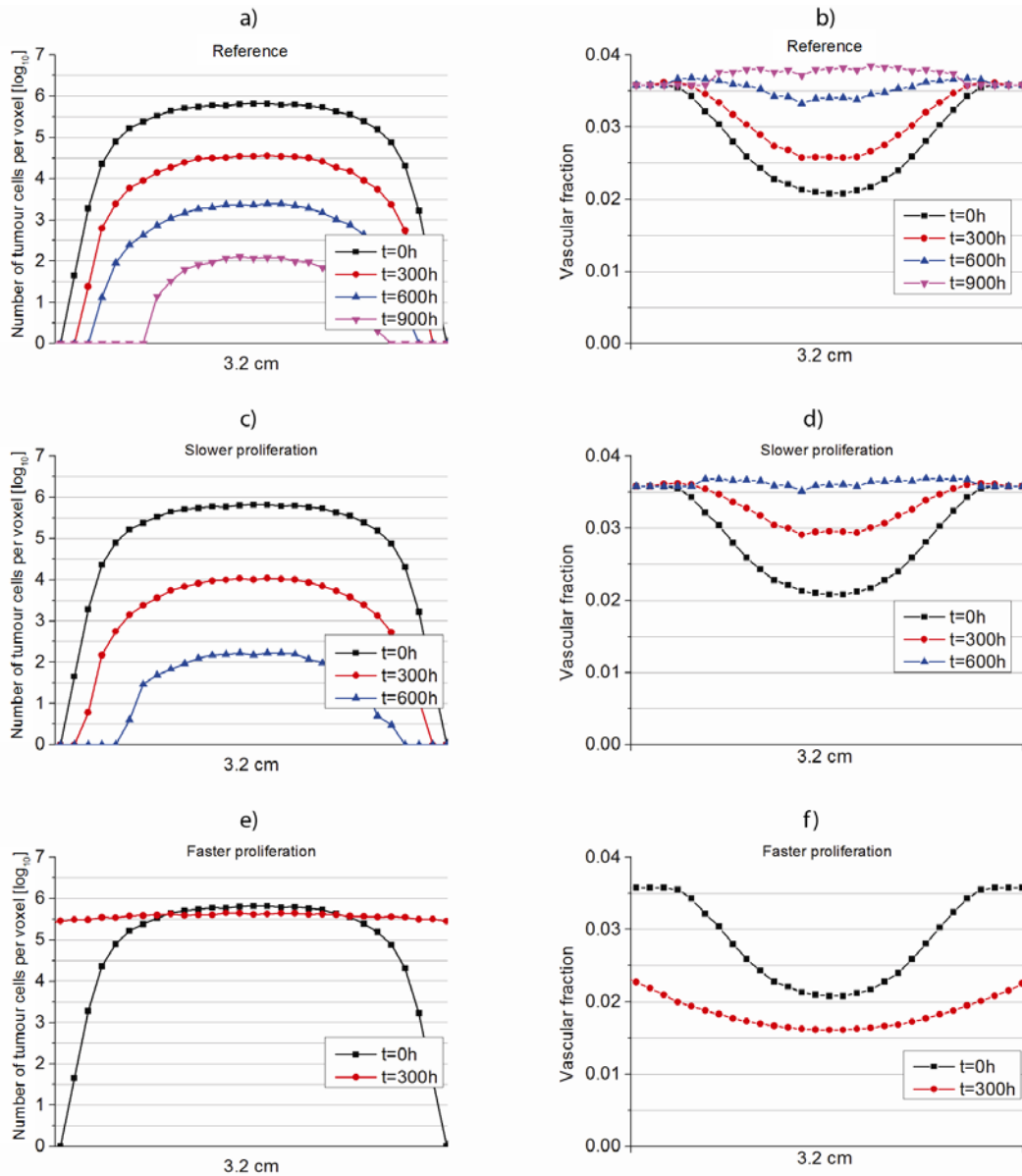


Figure 3.14: Profiles of tumour cell density (left) and vascular fraction (right) on a line through the centre of the virtual tumour during radiotherapy. The impact of considering slower (c and d) and faster (e and f) proliferation of tumour cells is shown.

Figure 3.15 shows the results of changing the half time of the resorption of dead cells. For this, t_r was scaled by the factors 2 and $\frac{1}{2}$, simulating slower and faster resorption, respectively. No significant changes were observed in tumour cell density. Noticeable changes are observed, however, in the vascular fraction. When the resorption is slower, substantially smaller values of vascular fraction are obtained, and vice versa, showing again the great dependence of vascular fraction on tumour shrinkage.

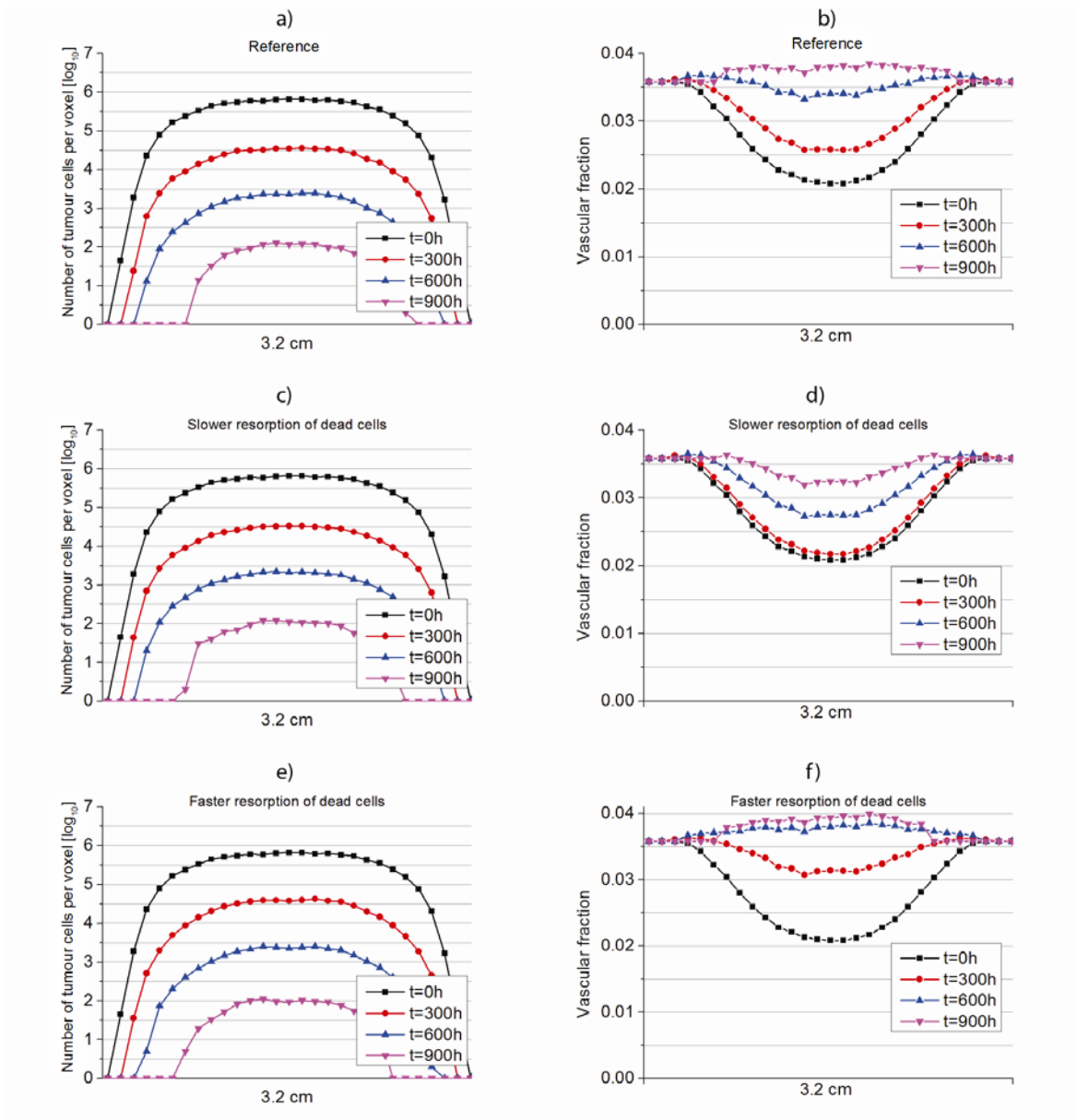


Figure 3.15: Profiles of tumour cell density (left) and vascular fraction (right) on a line through the centre of the virtual tumour during radiotherapy. The impact of considering slower (c and d) and faster (e and f) resorption of dead cells is shown.

3.2.3 Tumour control probability

Figure 3.16 displays the TCP-curve for two simulated tumours having different vascular fractions. The red curve in Figure 3.16 is the simulated TCP curve of the hypoxic virtual tumour used as reference in the previous sections (vascular fraction 3.6%). The tolerance dose TD_{50} is 71 Gy, which is within the range of values published by Yaromina *et al.* [77] for human SCCs. The simulated TCP curve for a well-oxygenated tumour (vascular fraction 7.2%) is shown as well (black curve). As compared to the hypoxic case, the curve is shifted to the left by 18 Gy, showing a TD_{50} of 53.6 Gy.

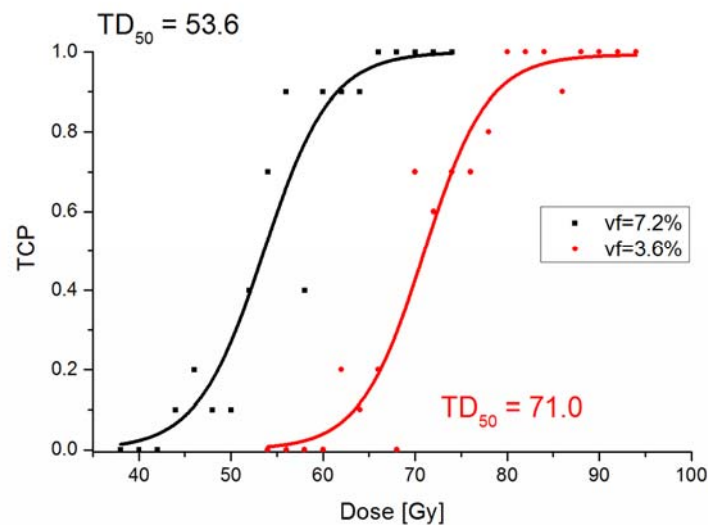


Figure 3.16: TCP curves simulated for a tumour with two different levels of hypoxia. The tumour corresponding to the black curve is much better oxygenated at the beginning of the simulated radiotherapy treatment than the one corresponding to the red curve.

3.2.4 Restricted proliferation capacity of very hypoxic tumour cells

Figure 3.17 shows the effect on tumour growth prior radiotherapy, if a reduced proliferative capacity of tumour cells with less than 2.5 mmHg of oxygen partial pressure is considered. Moderate changes in the vascular fraction are observed at the beginning ($t=300$ h). However, a clear effect on tumour size is noticed. Figure 3.18 shows the effect on tumour shrinkage during radiotherapy under the same conditions. Again, only a slight increase in the vascular fraction is observed in $t=300$ h. The effect on tumour size is markedly smaller than in the case of growth.

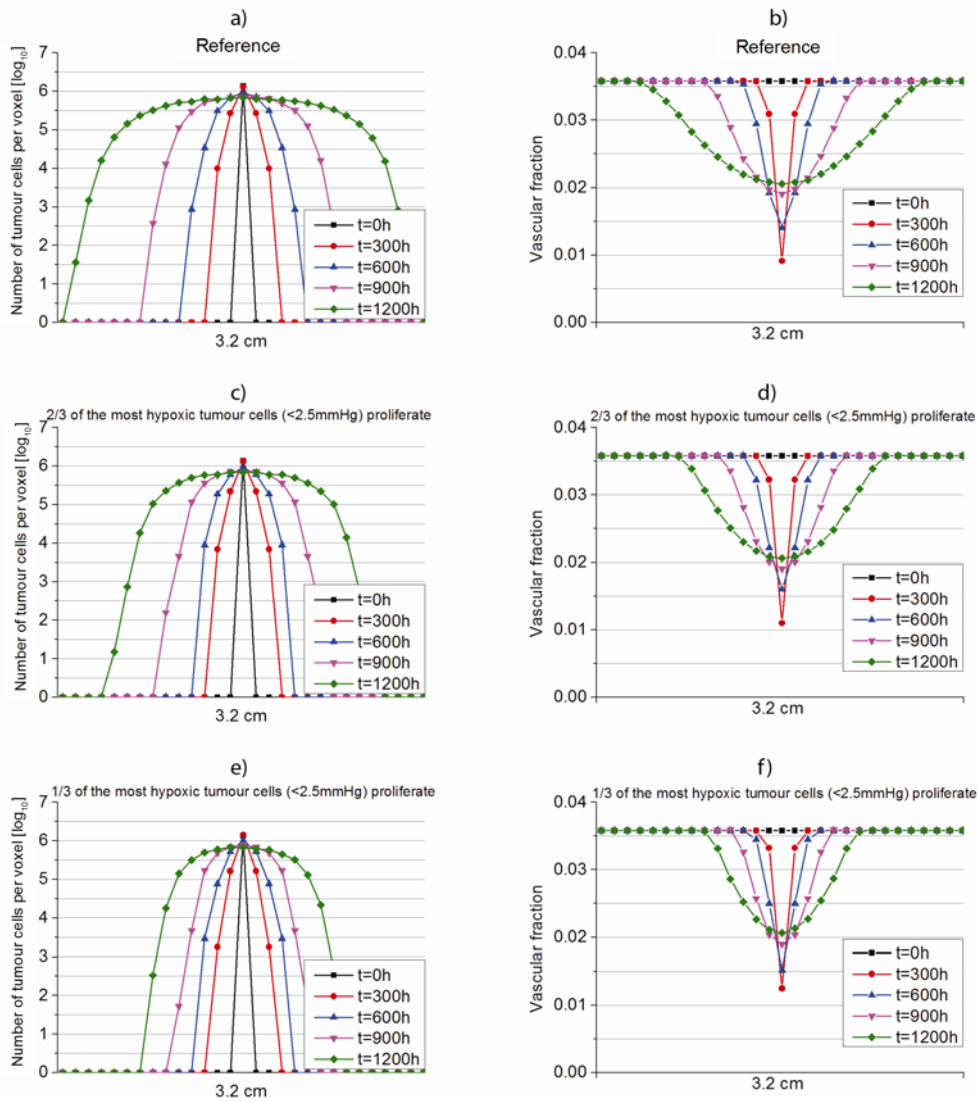


Figure 3.17: Profiles of tumour cell density (left) and vascular fraction (right) through the centre of the virtual tumour during tumour growth prior to radiotherapy. The impact of the reduced proliferation rate of very hypoxic cells ($< 2.5 \text{ mmHg}$) is shown.

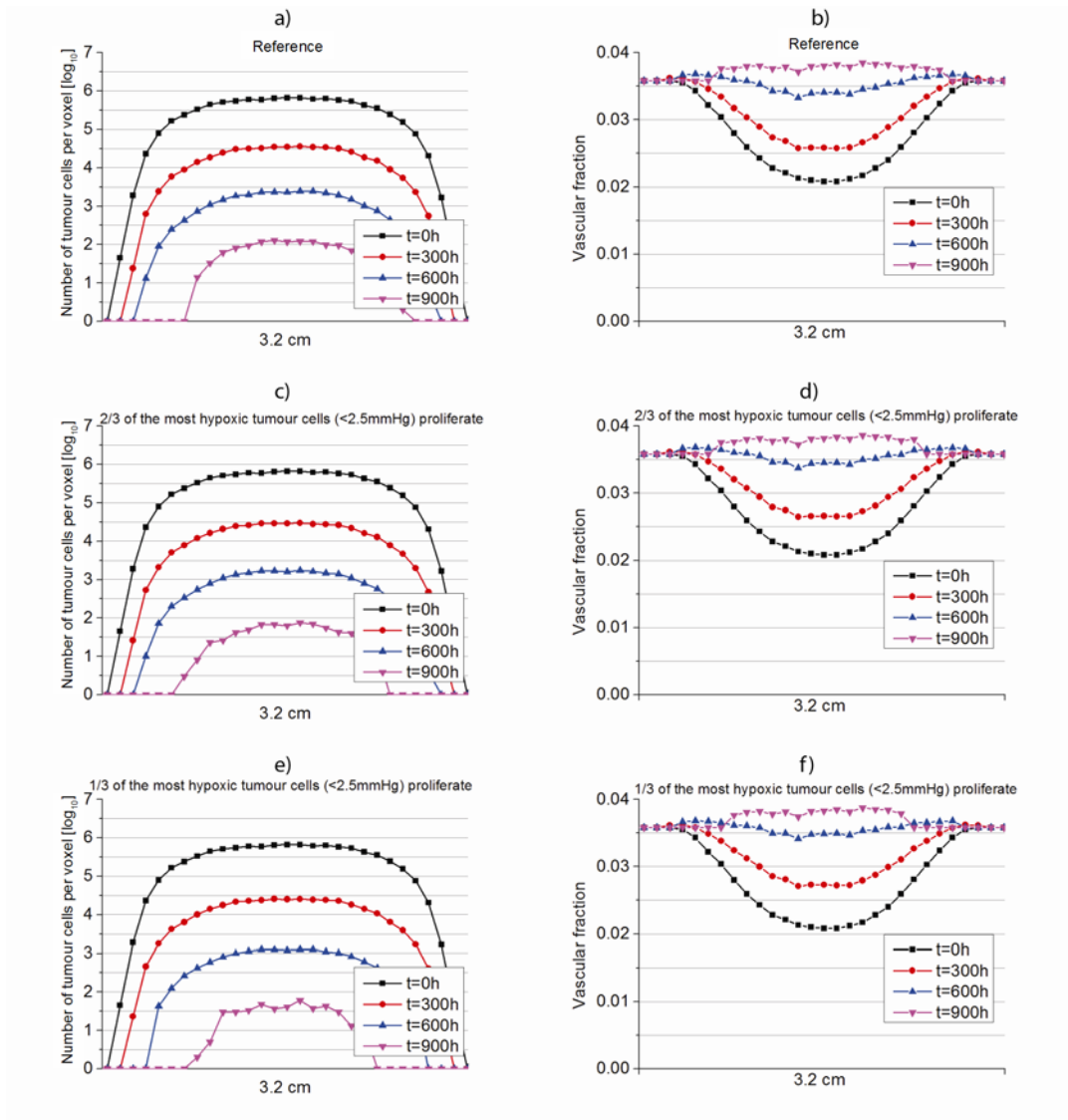


Figure 3.18: Profiles of tumour cell density (left) and vascular fraction (right) through the centre of a virtual tumour during radiotherapy. The impact of considering reduced proliferation of very hypoxic cells ($< 2.5 \text{ mmHg}$) is shown.

3.2.5 Redistribution of dose

As seen in the figures of the previous sections, the tumour has an initial vascular fraction of about 2.1% in the centre and 3.6% in the periphery. For these vascular fraction values, the cell survival fraction was calculated using the PO₂ histograms generated by the TOM and assuming several dose levels around 2 Gy. This is summarized in Figure 3.19, in which a linear fit was performed for each data set. For both vascular fraction values, the same survival fraction is obtained at doses of $2 \pm 0.082 \text{ Gy}$. Therefore, the dose values 2.082 Gy and 1.918 Gy were prescribed to the tumour core and tumour periphery, respectively, both regions having the same volume (half the total tumour volume). For this new dose distribution, which can be considered as an integrated boost, the corresponding TCP curve was simulated. The result is displayed in Figure 3.20 together with the previously

simulated TCP for the hypoxic tumour irradiated with a homogeneous dose distribution (red curve in Figure 3.16).

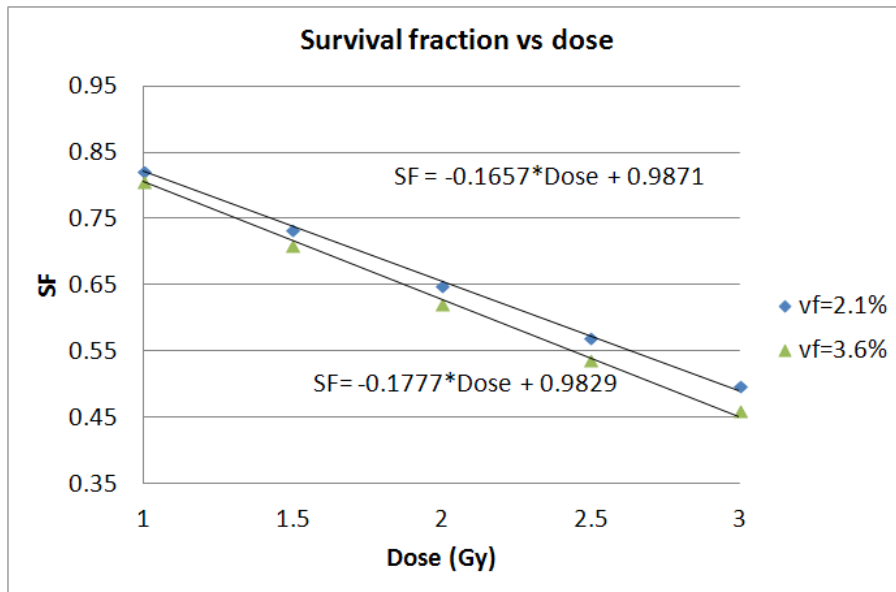


Figure 3.19: Dependence of the survival fraction on dose for two vascular fraction values.

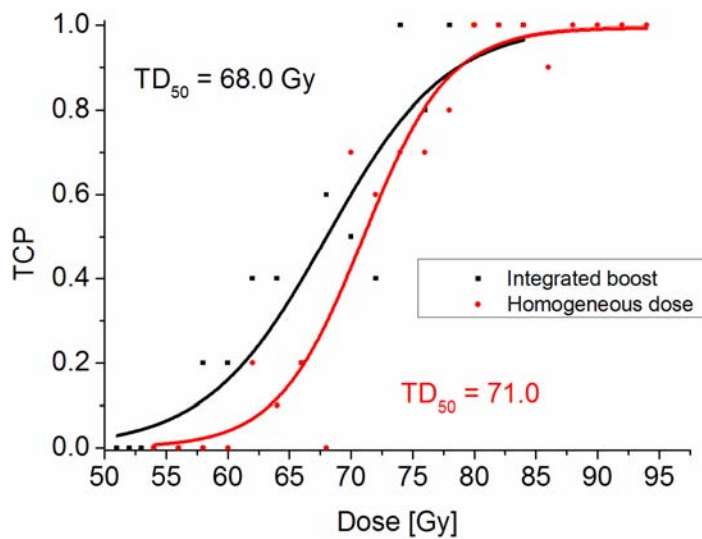


Figure 3.20: TCP-curves for the same tumour using a homogeneous dose distribution or an integrated boost, respectively. The red curve corresponds to the reference case shown in Figure 3.16.

4 Discussion

4.1 Tumour oxygenation model

4.1.1 Simulations

The PSE method has shown to be a suitable and easy to handle method to simulate oxygen distribution in tumours. Simulations of oxygen distributions in cases with simple geometries are in accordance with the results using other numerical methods used in the literature, and the simulated oxygen partial pressure radial profile around a single vessel shows good agreement with published results. The simulated maximum diffusion distance is in accordance with the values obtained by simulations of Daşu *et al.* (143 μm) [14], analytical calculations of Thomlinson and Gray (145 μm) [9] and experimental measurements of Thomlinson and Gray (in the range 100-200 μm) [9] and Olive *et al.* (in the range 107-193 μm) [32]. Although equation (2.11) can be also solved with other numerical methods, the PSE method was chosen because it is intuitive, computationally efficient and easily expandable to implement additional features, such as convection of fluids, complicated geometries and tracer dynamics in future studies.

Figure 3.2 shows that the oxygen histograms for point-like and linear vessels are very different. Considering that in nature vessels are elongated rather than point-like structures, the point-like approach underestimates the hypoxic fraction considerably and should not be used in this kind of simulations. In the same figure, it is shown that the 2D and 3D approaches give very similar oxygen histograms, confirming the assumptions of Daşu *et al.* [14], who considered that the 2D approach is a reasonable simplification, however, without showing computational comparisons. Due to the high computational effort of the 3D simulations, the 2D approach appears more suitable and was therefore preferred for all simulation studies.

The heterogeneity in the vessel distribution plays an important role for the simulated oxygen distributions, as shown in Figure 3.3. A completely random distribution gives the same oxygen distribution as a partially random one with a σ value comparable to IVD_0 , however, as the value of σ becomes smaller (less heterogeneity) the histograms indicate a much better oxygenation. This is in accordance with the well known fact that tumours show more hypoxia because of their chaotic vessel architecture [72], in contrast to the generally well oxygenated normal tissues, which have a more regular vascular architecture. From Figure 3.4, it can be seen that a more regular IVD distribution ($\sigma = IVD/4$, dotted line) leads to a larger mean IVD . Nevertheless, this leads to better and more homogeneous oxygenation of tissue for a given vascular fraction (Figure 3.3).

Figure 3.6 shows that the *IVD* distribution generated by the model using the completely randomly approach are in accordance with experimental data. Nevertheless, our model cannot reproduce the experimental curves perfectly. If we describe the *IVD* distributions by log-normal density functions, as done by Konerding *et al.*, the difference between the experimental and model-based curves is that the former has a larger dispersion factor, which means that the curves are slightly less symmetrical and their maximum is shifted somewhat to the left (as shown in Figure 3.6). An explanation for this disagreement may be that our simplified model does not consider exactly the same variables as those used to characterize the experimental vessel architecture. For the latter, varying vessel diameters and branching of vessels were additionally used. Furthermore, the description of the distances between vessels is not fully described by the *IVD* distribution, due to the fact that it only considers the distances to the nearest neighbour, ignoring for example the existence of larger regions with a smaller vessel density. So although the mean *IVD* is identical by construction, the shape of the simulated *IVD* distributions may still be somewhat different.

Another important consideration when comparing our measurements with the distributions measured by Konerding *et al.* is that if we select a *vf* according to the experimental mean *IVD*, we obtain values of around 1% or less (0.2% in the case of Figure 3.6), which correspond to simulated hypoxic fractions of 90% or larger. Although there are published measured oxygen histograms with similar large hypoxic fractions [6], the majority of pre-clinical studies show higher oxygenation levels and hence lower hypoxic fractions [78, 40]. Another example of this issue is that a mean *IVD* of around 300 μm was measured by Awwad *et al.* [2] in cervical carcinoma. This value is similar to those of Konerding *et al.*, which are associated with hypoxic fractions of more than 90%. In contrast, Ellingsen *et al.* [20] report lower hypoxic fractions of less than 50% for cervical carcinoma. These discrepancies should be explained by a better understanding and description of the vascular architecture, as discussed in the previous paragraph. For example, Dewhirst *et al.* [17] measured larger vessel diameters in some tumours (up to 84.9 μm) than the 20 μm considered in this work.

In our simulations we used an oxygen partial pressure of 40 mmHg in the vessels, which is considered to be a reasonable value by many authors [67, 60, 14, 42]. With this value our simulated oxygen histograms agree well with published measured [72, 40, 6, 36, 54, 63] and simulated [35, 13, 52, 71] data, in the sense that the PO_2 values are smaller than 40 mmHg, the oxygen distributions look similar and hypoxic fractions are in similar ranges. A precise quantitative comparison between our simulated and the published experimental PO_2 histograms was not possible, since no correspondence between histograms and vascular fraction are given in the literature.

Some authors also report measured oxygen histograms which are shifted to much higher values, close to the oxygen partial pressure in arteries (80-100 mmHg) [72, 78, 40, 36]. This could be explained through a direct connection of some tumour vessels to pre-existing well oxygenated host arterioles. By selecting a higher intravascular oxygen partial pressure, the model can reproduce these histograms as well, as shown in Figure 4.1.

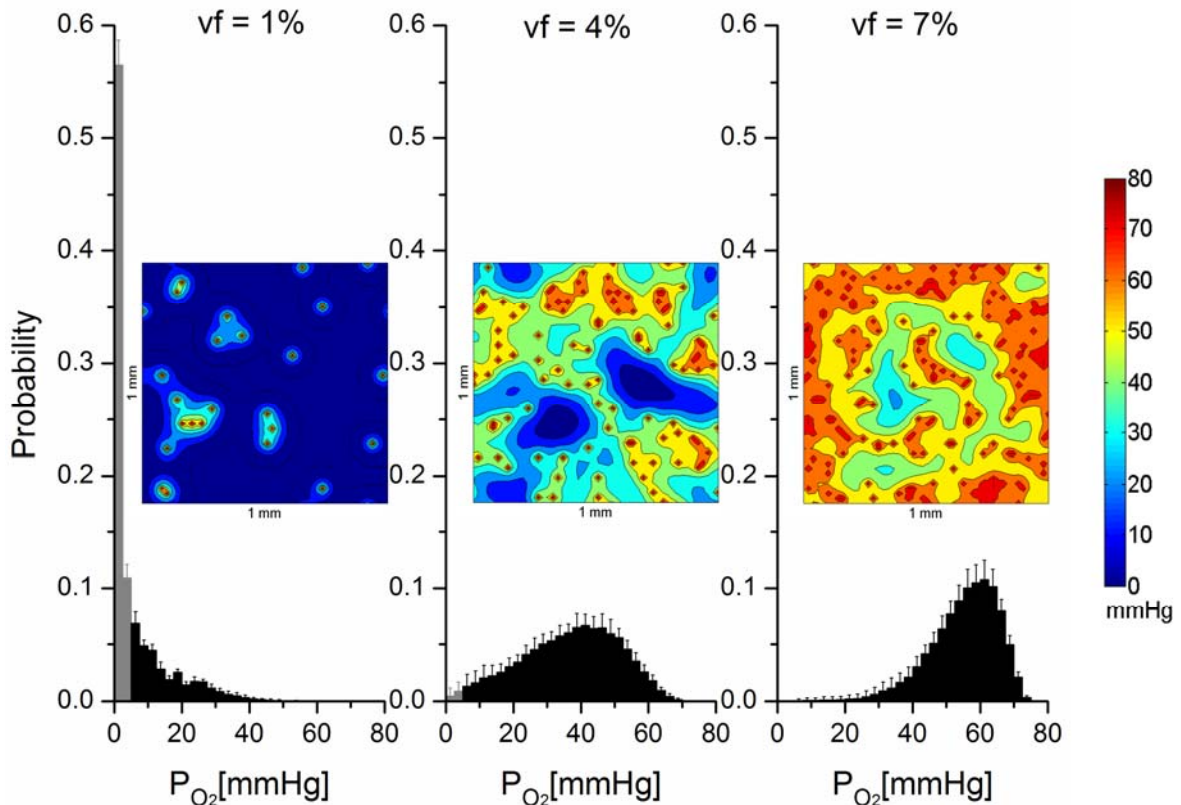


Figure 4.1: Simulated oxygen distributions and histograms for different vascular fractions (1%, 4% and 7%, from left to right) using the parallel linear vessels approach and an intravascular oxygen partial pressure of 80 mmHg. The grey bins in the histograms mark the hypoxic fraction. Error bars of the bins of the histograms indicate the standard deviation of repeated simulations ($n=20$).

4.1.2 Model assumptions

When using our model to predict the oxygenation in tumours, it has to be considered that the model is based on assumptions of the vascular fraction, the vessel diameter, the vessel architecture and its heterogeneity as well as the intravascular oxygen concentration. Using the vascular fraction as a measure of blood volume seems reasonable as the blood volume is at least one essential parameter determining the oxygen transport to the tissue. At least in principle, the blood volume is accessible as a fitting parameter of the time activity curve for a specific tumour region (e.g. a tumour voxel) in dynamic PET imaging, when using the two-tissue compartmental model [74]. Preliminary results, however, show great variability for this parameter and values differ from those obtained in histology experiments [74, 65, 18], so further developments are needed here. Alternatively, vascular fraction values can be obtained from MRI as well.

Many studies have been published in the last decade in which blood volume or vascular density is measured using different MR techniques. As an example, Wu *et al.* [76] measured microvessel densities in mouse brain using an iron oxide contrast agent and obtained good agreement with histological experiments. A second example is the work by Bremer *et al.* [8], in which vascular fraction values between 2.1 and 6.6% were obtained for different experimental tumours. These values showed good agreement with other experiments as well. It has to be noted that the vascular fraction values obtained either from PET or from MRI correspond to a tumour subvolume or voxel, respectively. In principle, this would allow to generate 3D-maps of this parameter. For a given vascular fraction of a selected voxel, the number of vessels is then defined by the vessel diameter. Although the value of this parameter may vary in real tumours, at least the average number of vessels can be determined from the average vascular fraction.

In our study, we have shown that the vascular architecture may have important impact on the oxygen distribution. The vessel architecture should therefore be as realistic as possible. Although our model could in principle handle realistic vessel architectures, they can currently be measured only invasively (e.g. by histology) in animal models rather than non-invasively in patients. We therefore used a statistical approach by distributing linear vessels randomly over a voxel and showed that the *IVD* distribution agrees well with published measured data. Two of the architectures (2D and 3D) lead to essentially the same oxygen histograms. If one could show in the future that the 2D/3D architecture result in comparable oxygen histograms as a real vascular architecture (taken e.g. from a histological sample), this could contribute to the validation of the model and it may then be transferred with greater confidence to patients. This approach is supported by the negligible difference between the 2D and 3D simulations, which suggest that the exact vascular pattern is less important as long as the large vascular heterogeneity of tumours is maintained.

In addition to the above assumptions, it has to be noted that the oxygen distribution is additionally influenced by the perfusion of the vessels as well as by the oxygenation saturation of the blood, which both may change as a function of space and time. As a result acute hypoxia (hypoxemic or ischemic) may occur additionally to chronic hypoxia. With this respect, it has to be noted that our vessels have a fixed diameter, no branching, and do not form a vascular network. Rather, each voxel is treated independently by assigning a vascular fraction, preferentially determined from medical imaging. It is therefore not possible to extend our model by another model describing the dynamics of blood flow and oxygenation saturation based on basic physical principles. However, if these parameters can be measured by medical imaging, average values can be assigned to each voxel. This approach would allow initializing the model with input data from individual patients and to individualize treatment planning. Although this has not been done in the present study, we showed that the model is in principle also able to describe

simple cases of acute hypoxia and the results indicate that neglecting acute hypoxia could lead to an important underestimation of the hypoxic fractions. This approach is less fundamental as compared to a complete modelling of the hemodynamic, but it seems to be more practical and clinically reliable as it directly connects the model to data of individual patients. Similar to these limitations, also other physiological aspects such as vessel wall permeability, spatially-dependent non-isotropic diffusion or oxygen consumption for other than tumour cells are not addressed in our model. To predict the radiation response of tumours, however, a pragmatic approach with effective but patient-specific input data appears more important than modelling of all biological effects from first principles.

4.2 Tumour response model

The TRM has shown to be a good approach to model the appearance of hypoxia during tumour growth. Hypoxia appears in central tumour regions due to the fast proliferation of tumour cells and the inappropriate supply of oxygen, as a consequence of chaotic vascular architectures and insufficient angiogenesis [72, 64]. Realistic median hypoxic fractions are obtained [47] when the growth of a tumour, starting from a single voxel, is simulated until a size typical of clinical tumours is reached. For that, realistic values of cell density, proliferation rate (of tumour cells and capillary cells due to angiogenesis) and vascular fraction, together with the results obtained by the TOM, are considered. While the impact of considering extreme cases of angiogenesis (vanishing or very fast) is small (Figure 3.8), substantial changes are seen in the results when tumour cell proliferation rates are changed (Figure 3.9). Great impact on the oxygenation level is seen also when modified vascular fraction values for the initial tumour voxel and the surrounding normal tissue are used, e.g. the median hypoxic fraction was reduced from 38% to 2.4% when a vascular fraction of 7.2% was used instead of 3.6%. Therefore, an adequate choice of these two input parameters (tumour cell proliferation rate and vascular fraction of the initial voxel and of the surrounding normal tissue) is of major importance.

The TRM is also able to model properly relevant aspects of the response of tumours to radiotherapy. Using realistic radiobiological input parameters (cell density, proliferation rates, radiosensitivities and oxygenation levels) and fractionation schemes typically used in the clinical routine, realistic responses are obtained.

The simulations showed the appearance of reoxygenation after the start of radiotherapy. After studying the different possible mechanisms of this appearance, it was found that the most important factor contributing to an improvement in tumour oxygenation is tumour shrinkage. After each irradiation, the remaining dead cells are resorbed, leading to a decreasing cell density in the regions where the amount of dead cells is larger, which

are usually the central tumour regions. This initiates tumour shrinkage modelled as a transfer of cells from the tumour periphery to the central regions. As the periphery presents normally higher vascular fraction values, capillary cells are also transferred towards the tumour core. A second factor influencing reoxygenation is angiogenesis; however, its impact is relatively small. Finally, the impact of the reduced oxygen consumption rate due to the presence of dead cells resulted to be negligible. It has to be noted, that the decreased oxygenation shown in Figure 3.12 (b and c) at radiotherapy start is not an effect of angiogenesis or a reduced oxygen consumption rate, but an indirect effect of the absence of resorption of dead cells. As tumour cells proliferate, and since cells killed by radiation are not yet resorbed, the proportion of capillary cells with respect to the total number of cells decreases initially. With this respect, angiogenesis is not able to compensate this effect, since the proliferation of capillary cells is too slow.

The impact of considering extreme cases of angiogenesis (vanishing or very fast) during the simulation of the response to radiotherapy is moderate (Figure 3.13). Not considering angiogenesis leads to slightly smaller vascular fraction values, but noticeable less shrinkage. On the other side, faster angiogenesis leads to a very slight reduction of the tumour size. This shows that, although the effect is moderate, considering angiogenesis during radiotherapy may be relevant for the assessment of tumour control.

As in the case of tumour growth, the tumour size is highly dependent on the proliferation rate of tumour cells (Figure 3.14). A slow proliferation rate leads to a prompt tumour control (c), while a faster proliferation rate prevents the tumour to shrink at all (e). This is supported by the additional resultant higher (d) and lower (f) vascular fraction levels, respectively. Therefore, it is important to choose this parameter properly.

Changing the rate of resorption of dead cells has a negligible impact on the tumour size and distribution of tumour cell density (Figure 3.15). If a slower resorption rate is considered, smaller values of vascular fraction are obtained, because of a limited transport of capillary cells from the tumour periphery towards the tumour core. Nevertheless, this is not reflected by a slower decrease of the number of viable tumour cells. Similarly, when a faster resorption of dead cells is considered, no noticeable faster shrinkage takes place despite the higher vascular fraction. The dependence of tumour shrinkage on the rate of resorption is thus unimportant for values within the considered range. This makes the choice of this parameter less critical. As a consequence, the lack of experimental measurements of this parameter does not represent a relevant limitation to the model. To obtain visible effects on tumour shrinkage, extreme and unrealistic values of this parameter should be used.

A great difference in TCP was observed in Figure 3.16, where TCP curves corresponding to two tumours with different oxygenation levels are shown. This is a result of major

importance, since it shows that models of tumour response to radiotherapy *must* consider hypoxia. In fact, not considering hypoxia would lead to absolutely wrong response assessments.

As shown in Figure 3.17 for tumour growth and in Figure 3.18 for tumour response to radiotherapy, the impact of a reduced proliferating capacity of tumour cells with less than 2.5 mmHg of oxygen partial pressure available is not negligible when hypoxic tumours are simulated. Hockel and Vaupel [27] mentioned that tumour cells with level of oxygen partial pressure of more than 0.2-1 mmHg would proliferate normally, and lower oxygenation values lead to a limited proliferation capacity. Additionally, totally anoxic cells would not proliferate at all. A good understanding of the dependence of tumour cell proliferation on oxygenation status may therefore be relevant for the simulations, however, to our knowledge, there is no consensus and only very little information about this aspect in the literature.

Redistributing the dose can lead to better tumour responses, as shown in Figure 3.20. In this case, the responses to two very simple dose distributions were compared: (i) a homogenous dose distribution over the whole tumour and (ii) an integrated boost with an increased dose in the hypoxic core of the tumour and a reduced dose in the periphery. Both dose distributions resulted in the same integral dose. Although the difference between the two dose levels of the integrated boost was only 0.164 Gy, a decrease of 3 Gy in the values of TD_{50} was achieved when comparing to the case with a completely homogeneous dose distribution. Clinically, such an approach would not only lead to a better response of the tumour, but it would also result in a lower dose in the tumour periphery and hence in the adjacent normal tissue. This may help additionally to reduce the risk of normal tissue complications or alternatively to increase the dose to the tumour. This example motivates the development of more elaborated procedures to redistribute dose according to the distribution of oxygen in tumours. This type of redistribution of dose is usually termed as “dose painting by numbers” [69]. An ideal approach would consider an optimization procedure, which maximizes the tumour response by choosing different dose levels for each tumour voxel, taking into account the oxygenation information contained in the respective PO₂ histograms.

4.3 Methods for validation

The TRM as well as the TOM is based on several assumptions and requires a number of input parameters of which some are still difficult to determine in patients. Therefore, prior to clinical application, the model has to be further validated with experimental and clinical data.

The TOM may be validated by means of animal experiments. For example, immunohistochemical procedures can be used to characterize vascular architecture, perfusion and hypoxia in different tumour types [44]. The vascular architecture can be measured using the endothelial marker CD31 in multiple adjacent cryosections. Similarly, to measure perfusion and hypoxia the markers Hoechst 33342 and pimonidazole can be used, respectively [44]. Knowing the vascular architecture and the perfused areas, the vascular fraction may be assessed and correlated to measured hypoxic fractions. Additionally, direct in-vivo measurements of oxygen partial pressure in different points within the tumour can be made by means of polarographic electrodes, which is currently considered as a gold standard for oxygenation measurements [23].

However, to measure the oxygen content in each tumour vessel and the distribution of PO₂ in experimental tumours on a microscopic scale represents still a major experimental challenge. For clinical application, it is also clear that the availability of histological and polarographic data in patients is limited and even if they were available, they would not represent 3D-distributions of the required parameters. Nevertheless, experimental data of this type could be used to validate calculations by the TOM and to investigate especially if the assumed simplified vascular architecture is sufficient for an adequate description of tumour oxygenation. If this could be shown, the vascular fraction together with a randomly-generated vascular heterogeneity would remain the most important input parameters, which may then be determined by non-invasive 3D imaging in the future. But even in this case, additional information on perfusion and intra-vascular oxygen content has to be included to describe acute hypoxia. This requires future developments in the field of 3D medical imaging. If these developments would be achieved, the TOM may be used with greater confidence in the TRM, which then has to be validated on his own.

The TRM may be validated by dose response experiments in experimental tumour systems, for example by irradiating implanted tumours in rats with different fractionation schemes and by investigating the impact of treatment and tumour-specific parameters on tumour control and volumetric changes. Such dose response experiments have been performed e.g. by Peschke *et al.* [51] and Karger *et al.* [29]. Prior to and during the irradiations, the shape of the tumour, the distribution of vascular fraction and tumour cell density as well as the hypoxic fraction should be measured histologically as well as by CT, PET or MR imaging techniques.

The experimental validation has to be accompanied by clinical examinations of the model. Clinical investigations, however, face the problem that usually only limited information is available. This requires clearly defined endpoints, detectable in patients and predictable by the TRM, so a correlation of model predictions with clinical outcome is possible. Also a correlation of predictions of the TOM with 3D imaging results is of high importance. With

this respect, applications of the model within clinical studies on hypoxia are desirable, as the acquired clinical information is maximized in this case.

4.4 Potential clinical application

Assuming the validation has been performed successfully, the TRM opens several possibilities to optimize radiotherapy treatments. One of them is to assess tumour control prior to radiotherapy for different treatment parameters and to select the potentially best treatment plan. Examples of such treatment parameters may include the fractionation schedule (hyper- or hypofractionation) or modified dose levels or dose distributions. Another possibility would be to predict the spatio-temporal development of hypoxic regions as well as the potential appearance of reoxygenation. The results of such simulations may have clinical impact on the decision whether an additional boost treatment is reasonable and which may be the optimal boost volume and time point to start the boost treatment.

In both cases, the possibility of implementing “dose painting” approaches appears particularly promising. Current dose delivery techniques like IMRT allow already the delivery of nearly arbitrary dose distributions, which could then be optimized according to the predictions of the TRM. This may especially advantageous for hypoxic tumours, as the TRM considers the oxygen distribution on a microscopic scale. It therefore considers the extremely high radioresistance of a few very hypoxic cells, which may cause treatment failure. Such a small hypoxic fraction would be ignored, if only average oxygenation values would be considered.

This special feature of the TRM is feasible due to the applied multi-scale approach. With this respect, the TRM considers two different scales: (i) the microscopic scale of the TOM, on which oxygenation distribution is simulated on a cell-by-cell resolution, and, (ii) the voxel-scale of the TRM on which the tumour response is simulated. For the latter, the oxygen distribution is condensed in voxel-specific PO₂ histograms allowing computationally efficient simulations of tumours with diameters of several centimetres containing thousands of voxels. By condensing the oxygenation by PO₂-histograms, the spatial orientation of the cells within each voxel is lost. This, however, is uncritical as the voxel size complies with the spatial resolution of 3D medical imaging as well as with that of the calculated and delivered dose distribution. On the other hand, the fraction of hypoxic cells, which is most important for the tumour response, is maintained in the TRM. In this way the most important information from the microscopic scale is transferred to the voxel-scale. Results of the simulations are then also obtained on two scales as a function of time: (i) the voxel-scale (e.g. vascular fractions, cell densities, PO₂-histograms and associated hypoxic fractions), and (ii) the macroscopic scale (e.g. tumour size, local

tumour control). Both of these scales are important for clinical assessments of the response to radiation therapy.

The described clinical applications of the TRM are limited by the fact that the TRM requires a biological characterization of the tumour prior to radiotherapy. This poses a challenge to the development of medical imaging techniques, which mostly determine surrogates of the required parameters rather than the parameters themselves. In addition, the longer the time interval for which the biological effects are predicted, the more likely is the necessity that additional effects have to be included in the TRM. A possible way to avoid this drawback is to update the tumour status from time to time by additional imaging.

As improving radiotherapy is always a matter of optimizing the differential response between the tumour and the surrounding normal tissue, the model would be strengthened, if the radiation response of normal tissue would also be included in the model. As the architecture of normal tissues differs considerably from that of tumours, this requires the modelling of the response based on functional subunits rather than on single cells [56].

5 Conclusions

In this work a radiobiological model (termed TRM) was developed, which simulates the growth and the response of tumours to radiotherapy considering patient-specific information of the tumour. It may help to improve the optimization of the radiation treatment, which is currently based only on the absorbed dose distribution and the clinical experience of the radiation oncologist.

Special emphasis was put on the characterization of the tumour oxygenation, which is of major importance for the prediction of the response of hypoxic tumours to radiotherapy, since they are known to be highly radioresistant. For this characterization, a complementary oxygenation model (termed TOM) was developed to simulate the microscopic oxygen distribution in each voxel, using as input parameter the respective vascular fraction.

In the developed model, processes on different scales are combined. The information on oxygenation, obtained by the TOM at the microscopic scale, is condensed to oxygen histograms and incorporated into the TRM. In this way, the tumour response can be calculated without referring to the microscopic scale, which would be computationally not feasible. This makes the model in principle applicable to clinical tumours and the characterization of the status of the tumour prior to radiotherapy may be performed by non-invasive 3D medical imaging techniques.

A promising future application of the model would be the development of dose painting techniques that optimizes tumour control by considering a detailed description of the radiation response of each tumour voxel.

The promising results obtained in this work motivate the future implementation and clinical application of the model. Prior to this, however, the model has to be further validated with experimental and clinical data, using e.g. the methods proposed in this work.

6 Bibliography

- [1] Alper T and Howard-Flanders P 1956 Role of oxygen in modifying the radiosensitivity of *E. coli* B *Nature* **178** 978-9
- [2] Awwad H K, el Naggat M, Mocktar N and Barsoum M 1986 Intercapillary distance measurement as an indicator of hypoxia in carcinoma of the cervix uteri *International journal of radiation oncology, biology, physics* **12** 1329-33
- [3] Baete S H, Vandecasteele J and De Deene Y 2011 19F MRI oximetry: simulation of perfluorocarbon distribution impact *Phys Med Biol* **56** 2535-57
- [4] Bayer C, Shi K, Astner S T, Maftai C A and Vaupel P 2011 Acute versus chronic hypoxia: why a simplified classification is simply not enough *Int J Radiat Oncol Biol Phys* **80** 965-8
- [5] Borkenstein K, Levegrun S and Peschke P 2004 Modeling and computer simulations of tumor growth and tumor response to radiotherapy *Radiat Res* **162** 71-83
- [6] Braun R D, Lanzen J L, Snyder S A and Dewhirst M W 2001 Comparison of tumor and normal tissue oxygen tension measurements using OxyLite or microelectrodes in rodents *Am J Physiol Heart Circ Physiol* **280** H2533-44
- [7] Bray F, Jemal A, Grey N, Ferlay J and Forman D 2012 Global cancer transitions according to the Human Development Index (2008-2030): a population-based study *The lancet oncology* **13** 790-801
- [8] Bremer C, Mustafa M, Bogdanov A, Jr., Ntziachristos V, Petrovsky A and Weissleder R 2003 Steady-state blood volume measurements in experimental tumors with different angiogenic burdens a study in mice *Radiology* **226** 214-20
- [9] Cardenas-Navia L I, Mace D, Richardson R A, Wilson D F, Shan S and Dewhirst M W 2008 The pervasive presence of fluctuating oxygenation in tumors *Cancer research* **68** 5812-9
- [10] Chapman J D 2003 Single-hit mechanism of tumour cell killing by radiation *International journal of radiation biology* **79** 71-81
- [11] Chow D C, Wenning L A, Miller W M and Papoutsakis E T 2001 Modeling pO₂ distributions in the bone marrow hematopoietic compartment. I. Krogh's model *Biophys J* **81** 675-84
- [12] Cottet G H and Koumoutsakos P 2000 *Vortex methods: theory and practice*: Cambridge University Press)
- [13] Daşu A, Toma-Daşu I and Karlsson M 2005 The effects of hypoxia on the theoretical modelling of tumour control probability *Acta Oncol* **44** 563-71
- [14] Daşu A, Toma-Daşu I and Karlsson M 2003 Theoretical simulation of tumour oxygenation and results from acute and chronic hypoxia *Phys Med Biol* **48** 2829-42
- [15] Degond P and Mas-Gallic S 1989 The Weighted Particle Method for Convection-Diffusion Equations. Part 1: The Case of an Isotropic Viscosity *Mathematics of Computation* **53** 485-507
- [16] Denekamp J 1982 Endothelial cell proliferation as a novel approach to targeting tumour therapy *British journal of cancer* **45** 136-9
- [17] Dewhirst M W, Tso C Y, Oliver R, Gustafson C S, Secomb T W and Gross J F 1989 Morphologic and hemodynamic comparison of tumor and healing normal

- tissue microvasculature *International journal of radiation oncology, biology, physics* **17** 91-9
- [18] Dimitrakopoulou-Strauss A, Strauss L G, Heichel T, Wu H, Burger C, Bernd L and Ewerbeck V 2002 The role of quantitative F-18-FDG PET studies for the differentiation of malignant and benign bone lesions *Journal of Nuclear Medicine* **43** 510-8
- [19] Dionysiou D D, Stamatakos G S, Uzunoglu N K, Nikita K S and Marioli A 2004 A four-dimensional simulation model of tumour response to radiotherapy in vivo: parametric validation considering radiosensitivity, genetic profile and fractionation *J Theor Biol* **230** 1-20
- [20] Ellingsen C, Ovrebo K M, Galappathi K, Mathiesen B and Rofstad E K 2012 pO(2) fluctuation pattern and cycling hypoxia in human cervical carcinoma and melanoma xenografts *International journal of radiation oncology, biology, physics* **83** 1317-23
- [21] Fassnacht D and Portner R 1999 Experimental and theoretical considerations on oxygen supply for animal cell growth in fixed-bed reactors *J Biotechnol* **72** 169-84
- [22] Folarin A A, Konerding M A, Timonen J, Nagl S and Pedley R B 2010 Three-dimensional analysis of tumour vascular corrosion casts using stereoinaging and micro-computed tomography *Microvasc Res* **80** 89-98
- [23] Gagel B, Reinartz P, Dimartino E, Zimny M, Pinkawa M, Maneschi P, Stanzel S, Hamacher K, Coenen H H, Westhofen M, Bull U and Eble M J 2004 pO(2) Polarography versus positron emission tomography ([¹⁸F] fluoromisonidazole, [¹⁸F]-2-fluoro-2'-deoxyglucose). An appraisal of radiotherapeutically relevant hypoxia *Strahlentherapie und Onkologie : Organ der Deutschen Rontgengesellschaft ... [et al]* **180** 616-22
- [24] Gray L H, Conger A D, Ebert M, Hornsey S and Scott O C A 1953 The Concentration of Oxygen Dissolved in Tissues at the Time of Irradiation as a Factor in Radiotherapy *Brit J Radiol* **26** 638-48
- [25] Hall E J 2000 *Radiobiology for the radiologist* (Philadelphia: Lippincott Williams & Wilkins)
- [26] Harting C, Peschke P, Borkenstein K and Karger C P 2007 Single-cell-based computer simulation of the oxygen-dependent tumour response to irradiation *Phys Med Biol* **52** 4775-89
- [27] Hockel M and Vaupel P 2001 Tumor hypoxia: definitions and current clinical, biologic, and molecular aspects *Journal of the National Cancer Institute* **93** 266-76
- [28] Joiner M and Kogel A v d 2009 *Basic clinical radiobiology* (London: Hodder Arnold)
- [29] Karger C P, Peschke P, Scholz M, Huber P E and Debus J 2013 Relative Biological Effectiveness of Carbon Ions in a Rat Prostate Carcinoma In Vivo: Comparison of 1, 2, and 6 Fractions *International journal of radiation oncology, biology, physics*
- [30] Kelly C J and Brady M 2006 A model to simulate tumour oxygenation and dynamic [¹⁸F]-Fmiso PET data *Phys Med Biol* **51** 5859-73
- [31] Kimura H, Braun R D, Ong E T, Hsu R, Secomb T W, Papahadjopoulos D, Hong K and Dewhirst M W 1996 Fluctuations in red cell flux in tumor microvessels can lead to transient hypoxia and reoxygenation in tumor parenchyma *Cancer research* **56** 5522-8
- [32] Kohandel M, Kardar M, Milosevic M and Sivaloganathan S 2007 Dynamics of tumor growth and combination of anti-angiogenic and cytotoxic therapies *Phys Med Biol* **52** 3665-77

- [33] Konerding M A, Fait E and Gaumann A 2001 3D microvascular architecture of pre-cancerous lesions and invasive carcinomas of the colon *British journal of cancer* **84** 1354-62
- [34] Konerding M A, Malkusch W, Klapthor B, van Ackern C, Fait E, Hill S A, Parkins C, Chaplin D J, Presta M and Denekamp J 1999 Evidence for characteristic vascular patterns in solid tumours: quantitative studies using corrosion casts *British journal of cancer* **80** 724-32
- [35] Lagerlof J H, Kindblom J, Cortez E, Pietras K and Bernhardt P 2013 Image-based 3D modeling study of the influence of vessel density and blood hemoglobin concentration on tumor oxygenation and response to irradiation *Med Phys* **40** 024101
- [36] Lyng H, Sundfor K and Rofstad E K 1997 Oxygen tension in human tumours measured with polarographic needle electrodes and its relationship to vascular density, necrosis and hypoxia *Radiother Oncol* **44** 163-9
- [37] Lyng H, Tanum G, Evensen J F and Rofstad E K 1999 Changes in oxygen tension during radiotherapy of head and neck tumours *Acta Oncol* **38** 1037-42
- [38] Malaise E P, Fertil B, Chavaudra N and Guichard M 1986 Distribution of radiation sensitivities for human tumor cells of specific histological types: comparison of in vitro to in vivo data *International journal of radiation oncology, biology, physics* **12** 617-24
- [39] Mayles P, Nahum A and Rosenwald J C 2007 Handbook of Radiotherapy Physics, Theory and Practice. Taylor & Francis)
- [40] Menon C, Polin G M, Prabakaran I, Hsi A, Cheung C, Culver J P, Pingpank J F, Sehgal C S, Yodh A G, Buerk D G and Fraker D L 2003 An integrated approach to measuring tumor oxygen status using human melanoma xenografts as a model *Cancer Res* **63** 7232-40
- [41] Merriam-Webster.com 2013 <http://www.merriam-webster.com>
- [42] Mönnich D, Troost E G, Kaanders J H, Oyen W J, Alber M and Thorwarth D 2011 Modelling and simulation of [18F]fluoromisonidazole dynamics based on histology-derived microvessel maps *Phys Med Biol* **56** 2045-57
- [43] Mönnich D, Troost E G, Kaanders J H, Oyen W J, Alber M and Thorwarth D 2012 Modelling and simulation of the influence of acute and chronic hypoxia on [18F]fluoromisonidazole PET imaging *Phys Med Biol* **57** 1675-84
- [44] Morchel P, Melkus G, Yaromina A, Zips D, Baumann M, Jakob P M and Flentje M 2010 Correlating quantitative MR measurements of standardized tumor lines with histological parameters and tumor control dose *Radiotherapy and oncology : journal of the European Society for Therapeutic Radiology and Oncology* **96** 123-30
- [45] Nahum A E, Movsas B, Horwitz E M, Stobbe C C and Chapman J D 2003 Incorporating clinical measurements of hypoxia into tumor local control modeling of prostate cancer: implications for the alpha/beta ratio *International journal of radiation oncology, biology, physics* **57** 391-401
- [46] Niemierko A 1998 Radiobiological models of tissue response to radiation in treatment planning systems *Tumori* **84** 140-3
- [47] Nordmark M, Bentzen S M, Rudat V, Brizel D, Lartigau E, Stadler P, Becker A, Adam M, Molls M, Dunst J, Terris D J and Overgaard J 2005 Prognostic value of tumor oxygenation in 397 head and neck tumors after primary radiation therapy. An international multi-center study *Radiother Oncol* **77** 18-24

- [48] Nordmark M, Hoyer M, Keller J, Nielsen O S, Jensen O M and Overgaard J 1996 The relationship between tumor oxygenation and cell proliferation in human soft tissue sarcomas *Int J Radiat Oncol Biol Phys* **35** 701-8
- [49] Olive P L, Vikse C and Trotter M J 1992 Measurement of oxygen diffusion distance in tumor cubes using a fluorescent hypoxia probe *Int J Radiat Oncol Biol Phys* **22** 397-402
- [50] Palacic B and Skarsgard L D 1984 Reduced oxygen enhancement ratio at low doses of ionizing radiation *Radiat Res* **100** 328-39
- [51] Peschke P, Karger C P, Scholz M, Debus J and Huber P E 2011 Relative biological effectiveness of carbon ions for local tumor control of a radioresistant prostate carcinoma in the rat *International journal of radiation oncology, biology, physics* **79** 239-46
- [52] Petit S F, Dekker A L, Seigneuric R, Murrer L, van Riel N A, Nordmark M, Overgaard J, Lambin P and Wouters B G 2009 Intra-voxel heterogeneity influences the dose prescription for dose-painting with radiotherapy: a modelling study *Phys Med Biol* **54** 2179-96
- [53] Podgorsak E B and International Atomic Energy Agency. 2005 *Radiation oncology physics : a handbook for teachers and students* (Vienna: International Atomic Energy Agency)
- [54] Pogue B W, Paulsen K D, O'Hara J A, Wilmot C M and Swartz H M 2001 Estimation of oxygen distribution in RIF-1 tumors by diffusion model-based interpretation of pimonidazole hypoxia and eppendorf measurements *Radiat Res* **155** 15-25
- [55] Price P, Sikora K and Illidge T 2008 *Treatment of cancer* (London: Hodder Arnold)
- [56] Rutkowska E, Baker C and Nahum A 2010 Mechanistic simulation of normal-tissue damage in radiotherapy--implications for dose-volume analyses *Phys Med Biol* **55** 2121-36
- [57] Sbalzarini I F 2011 Spatiotemporal Modeling and Simulation *Lecture notes for the course 'Spatiotemporal Modeling and Simulation' at ETH Zurich*
- [58] Schlegel W, Bortfeld T and Grosu A 2005 *New technologies in radiation oncology* (Berlin ; London: Springer)
- [59] Secomb T W, Hsu R, Dewhirst M W, Klitzman B and Gross J F 1993 Analysis of oxygen transport to tumor tissue by microvascular networks *Int J Radiat Oncol Biol Phys* **25** 481-9
- [60] Secomb T W, Hsu R, Ong E T, Gross J F and Dewhirst M W 1995 Analysis of the effects of oxygen supply and demand on hypoxic fraction in tumors *Acta Oncol* **34** 313-6
- [61] Secomb T W, Hsu R, Park E Y and Dewhirst M W 2004 Green's function methods for analysis of oxygen delivery to tissue by microvascular networks *Annals of biomedical engineering* **32** 1519-29
- [62] Smith K A, Hill S A, Begg A C and Denekamp J 1988 Validation of the fluorescent dye Hoechst 33342 as a vascular space marker in tumours *British journal of cancer* **57** 247-53
- [63] Star-Lack J M, Adalsteinsson E, Adam M F, Terris D J, Pinto H A, Brown J M and Spielman D M 2000 In vivo 1H MR spectroscopy of human head and neck lymph node metastasis and comparison with oxygen tension measurements *AJNR. American journal of neuroradiology* **21** 183-93
- [64] Steel G G 2002 *Basic clinical radiobiology* (London, New York: Arnold, Oxford University Press)

- [65] Strauss L G, Dimitrakopoulou-Strauss A and Haberkorn U 2003 Shortened PET data acquisition protocol for the quantification of ¹⁸F-FDG kinetics *Journal of nuclear medicine : official publication, Society of Nuclear Medicine* **44** 1933-9
- [66] Tang 1933 On the rate of oxygen consumption by tissues and lower organisms as a function of oxygen tension. *Q. Rev. Biol.* **8** 260-74
- [67] Tannock I F 1972 Oxygen diffusion and the distribution of cellular radiosensitivity in tumours *The British journal of radiology* **45** 515-24
- [68] Thomlinson R H and Gray L H 1955 The histological structure of some human lung cancers and the possible implications for radiotherapy *Br J Cancer* **9** 539-49
- [69] Thorwarth D, Eschmann S M, Paulsen F and Alber M 2007 Hypoxia dose painting by numbers: a planning study *International journal of radiation oncology, biology, physics* **68** 291-300
- [70] Titz B and Jeraj R 2008 An imaging-based tumour growth and treatment response model: investigating the effect of tumour oxygenation on radiation therapy response *Phys Med Biol* **53** 4471-88
- [71] Toma-Dașu I, Dașu A and Brahme A 2009 Dose prescription and optimisation based on tumour hypoxia *Acta Oncologica* 1-12
- [72] Vaupel P, Kallinowski F and Okunieff P 1989 Blood flow, oxygen and nutrient supply, and metabolic microenvironment of human tumors: a review *Cancer Res* **49** 6449-65
- [73] Verlet L 1967 Computer Experiments on Classical Fluids .I. Thermodynamical Properties of Lennard-Jones Molecules *Physical Review* **159** 98-&
- [74] Wang W, Georgi J C, Nehmeh S A, Narayanan M, Paulus T, Bal M, O'Donoghue J, Zanzonico P B, Schmidtlein C R, Lee N Y and Humm J L 2009 Evaluation of a compartmental model for estimating tumor hypoxia via FMISO dynamic PET imaging *Phys Med Biol* **54** 3083-99
- [75] Wouters B G and Brown J M 1997 Cells at intermediate oxygen levels can be more important than the "hypoxic fraction" in determining tumor response to fractionated radiotherapy *Radiation research* **147** 541-50
- [76] Wu E X, Tang H and Jensen J H 2004 High-resolution MR imaging of mouse brain microvasculature using the relaxation rate shift index Q *NMR Biomed* **17** 507-12
- [77] Yaromina A, Thames H, Zhou X, Hering S, Eicheler W, Dorfler A, Leichtner T, Zips D and Baumann M 2010 Radiobiological hypoxia, histological parameters of tumour microenvironment and local tumour control after fractionated irradiation *Radiotherapy and oncology : journal of the European Society for Therapeutic Radiology and Oncology* **96** 116-22
- [78] Zhao D, Ran S, Constantinescu A, Hahn E W and Mason R P 2003 Tumor oxygen dynamics: correlation of in vivo MRI with histological findings *Neoplasia* **5** 308-18

7 Acknowledgements

First and foremost, I would like to express my sincere gratitude to my supervisor Prof. Dr. Christian Karger for his constant support, motivation, patience, immense knowledge and the many constructive discussions.

I am also immensely grateful to Prof. Dr. Wolfgang Schlegel for being reviewer of this thesis and one of my examiners, for his support as the head of the Department of Medical Physics in Radiation Oncology and for his crucial role in the development of medical physics in Chile.

I would like to thank Prof. Dr. Ulrich Uwer and Prof. Dr. Joerg Jaeckel for being members of my examination committee and Dr. Gabriele Sroka-Perez for being part of my thesis advisory committee.

For his enthusiasm and valuable help in topics related to biology, especial thanks to Dr. Peter Peschke.

I would like to thank Maria Cristina Depassier for the trust put in me and Marcel Clerc for his encouraging and motivating words. Their support was relevant to my decision to follow a scientific career.

Thanks to my colleagues at the DKFZ, Andrés, Carine, Christin, Christine, Edgardo, Liu, Maria, Martina, Pamela, Sonja and Torsten, and to the medical physicists at the Heidelberg University Clinic, especially to Gerald Major for his enthusiasm in teaching me the different aspect of medical physics in the clinic.

Especial thanks to all my friends during my time in Heidelberg.

This work was supported by a grand of the Ministry of Education of Chile, Programa MECE Educación Superior (2).

Last but not least, I would like to thank Arturo, Carmen, María Elena, Palu and Tuni. This work is dedicated to them.